

Spring 2023

Modeling Excited State Processes in Molecular Aggregates by Constructing an Adaptive Basis For The Hierarchy of Pure States

Leonel Varvelo

Southern Methodist University, vleo32@gmail.com

Follow this and additional works at: https://scholar.smu.edu/hum_sci_chemistry_etds

 Part of the Biological and Chemical Physics Commons, Computational Chemistry Commons, Condensed Matter Physics Commons, Physical Chemistry Commons, and the Quantum Physics Commons

Recommended Citation

Varvelo, Leonel, "Modeling Excited State Processes in Molecular Aggregates by Constructing an Adaptive Basis For The Hierarchy of Pure States" (2023). *Chemistry Theses and Dissertations*. 35.
https://scholar.smu.edu/hum_sci_chemistry_etds/35

This Thesis is brought to you for free and open access by the Chemistry at SMU Scholar. It has been accepted for inclusion in Chemistry Theses and Dissertations by an authorized administrator of SMU Scholar. For more information, please visit <http://digitalrepository.smu.edu>.

MODELING EXCITED STATE PROCESSES IN MOLECULAR AGGREGATES
BY CONSTRUCTING AN ADAPTIVE BASIS FOR
THE HIERARCHY OF PURE STATES

Approved by:

Dr. Doran I.G.B. Raccah
Associate Professor

Dr. Devin Matthews
Associate Professor

Dr. Peng Tao
Associate Professor

MODELING EXCITED STATE PROCESSES IN MOLECULAR AGGREGATES
BY CONSTRUCTING AN ADAPTIVE BASIS FOR
THE HIERARCHY OF PURE STATES

A Dissertation Presented to the Graduate Faculty of the

Dedman College

Southern Methodist University

in

Partial Fulfillment of the Requirements

for the degree of

Master of Science

with a

Major in Chemistry

by

Leonel Varvelo

B.S., Physics, University of Houston

May 13, 2023

Copyright (2023)

Leonel Varvelo

All Rights Reserved

ACKNOWLEDGMENTS

I am grateful to the SMU chemistry department for their role in my professional development. I am also grateful to the SMU high performance computing team as the work presented in this thesis was performed using ManeFrame II. Special thanks to Dr. Robert Kalescky for always providing assistance.

I am grateful for all my lab members past and present, working with y'all was a greatly rewarding experience. I wish to express special gratitude to Jacob Lynd who is an author on all works presented here. Without his added support I would not have accomplished everything that I did. Additional thanks are needed for Mohamed Elrefaiy and Mayar Tarek Ibrahim for being wonderful friends and confidants.

My external gratitude goes to Dr. Raccah for taking me in as his first graduate student. His guidance was instrumental in my development as a scientist and overall human being. Without his enduring support and relentless faith in me I could not have overcome the challenges presented to me. I can never repay the debt I owe you but I look forward to trying.

Varvelo, Leonel

B.S., Physics, University of Houston

Modeling Excited State Processes in Molecular Aggregates
by Constructing an Adaptive Basis For
The Hierarchy of Pure States

Advisor: Dr. Doran I.G.B. Raccah

Master of Science degree conferred May 13, 2023

Dissertation completed April 26, 2023

Simulating excitation energy transfer (EET) in molecular materials is of crucial importance for the development of and understanding of materials such as organic photovoltaics and photosynthetic systems and further development of novel materials. The Hierarchy of Pure States (HOPS) is an exact framework for the time evolution of an open quantum system in which a hierarchy of stochastic wave functions are propagated in time. The adaptive HOPS (adHOPS) method achieves size-invariant scaling with the number of simulated molecules for sufficiently large aggregates by using an adaptive basis that moves with the excitation through the material. To demonstrate the power of the reduced scaling of ad-HOPS in realistic molecular materials we build a large hexagonally-packed supercomplex constructed of B850 rings from the photosynthetic antenna complex of purple bacteria, light harvesting 2 (LH2). We use adHOPS to simulate EET in the supercomplex to understand the mechanism of transport in LH2 and demonstrate that we can extract mechanistic insight about excited state process in molecule materials on an unprecedented scale.

TABLE OF CONTENTS

LIST OF FIGURES	viii
LIST OF TABLES	xii
CHAPTER	
1 Introduction	1
1.1. Closed Quantum Systems	1
1.2. Open Quantum Systems	3
1.3. Hamiltonian's	4
1.3.1. System Hamiltonian	4
1.3.2. Bath Hamiltonian	5
1.3.3. Interaction Hamiltonian	5
1.3.3.1. Correlation Function	6
2 Non-Markovian Systems	8
2.1. Non-Markovian Quantum State Diffusion	8
2.2. Hierarchy of Pure States	10
3 Results	16
3.1. Normalized Nonlinear HOPS	16
3.2. Locality in HOPS	22
3.3. Adaptive Algorithm	24
3.3.1. time-evolution	24
3.3.2. Basis Update Steps	26
3.4. Adaptive Basis	27
4 Application	32

4.1. Light Harvesting 2	32
-------------------------------	----

APPENDIX

A Matsubara Decomposition	41
---------------------------------	----

BIBLIOGRAPHY	42
--------------------	----

LIST OF FIGURES

Figure	Page
1.1 Schematic view of individual pigments in a linear chain	4
3.1 Magnitude of the first three auxiliaries in a single-mode HOPS calculation. (a)The magnitude of the auxiliaries calculated using the non-linear HOPS equation (darker lines correspond to higher k values). (b) The magnitude of the auxiliaries calculated using the non-linear HOPS equation with the k -dependent prefactor.....	22
3.2 Dynamic localization induced by coupling to the environment	22
3.3 Localization in a single HOPS trajectory.(a) Contour map of site populations in the physical wave function (darker is more populated). (b) Norm-squared of auxiliary wave functions for a two-dimensional subset of the hierarchy associated with site 2 (column) and 3 (row). Panels are labelled by their index vector (\vec{k}). The shaded region represents the time-period when site 2 is occupied. The physical wave function ($\vec{k} = 0$) shows the populations of site 2 and 3 as green and blue lines, respectively. Parameters: $V = 10 \text{ cm}^{-1}$, $\lambda = \gamma = 50 \text{ cm}^{-1}$, $T = 295 \text{ K}$, and $k_{max} = 10$	23
3.4 The adHOPS algorithm. (a) The overarching algorithm that an adaptive HOPS simulation follows. (b) The algorithm that updates the adaptive HOPS basis during update step	25
3.5 Comparing HOPS and adHOPS for a five-site linear chain. (a) Site 3 population dynamics for HOPS (black line) and adHOPS (green line). (b) Mean adaptive error as a function of δ . The grey region represents error beneath the statistical error for a 104 trajectory ensemble. (c) Ensemble distribution of the size of the adaptive auxiliary basis as a function of δ ...	27
3.6 Comparing dynamics and auxiliary basis size as a function electronic coupling (V) for the full (black) and adaptive (green) HOPS calculations. (a) Site 3 population dynamics when $k_{max10} = 10$. (b) Size of the auxiliary basis as a function of maximum hierarchy depth. Parameters: $V = 50 \text{ cm}^{-1}$, $\lambda = \gamma = 50 \text{ cm}^{-1}$, $T = 295 \text{ K}$, $k_{max} = 10$, and $N_{traj} = 10^4$	28

3.7	Advantageous scaling of adHOPS simulations for large numbers of pigments. Average number of elements in the adaptive system (top) and auxiliary (bottom) basis for linear chains of different lengths. Other parameters: $\lambda = \gamma = 50 \text{ cm}^{-1}$, $T = 295 \text{ K}$, $\delta = 10^{-3}$, and $N_{\text{traj}} = 10^4$. For $V = 250 \text{ cm}^{-1}$, $\gamma_{\text{mark}} = 1000 \text{ cm}^{-1}$, all others used $\gamma_{\text{mark}} = 500 \text{ cm}^{-1}$	29
3.8	Average CPU time for HOPS (black squares) and adHOPS (green circles). The green line in the right panel shows a linear fit to the data from $N_{\text{pig}}=16$ to 1000, with a coefficient of 0.0277. Calculations were run using Intel Xeon 2.1 GHz processor. Parameters: $V = 50 \text{ cm}^{-1}$, $\lambda = \gamma = 50 \text{ cm}^{-1}$, $T = 295 \text{ K}$, $k_{\max} = 10$, $\delta = 3 \times 10^{-4}$ and $N_{\text{traj}} = 10^4$	30
3.9	Exciton diffusion coefficient (in units of molecular spacing, l_0) for a 10^3 pigment chain from a linear fit to the mean-squared displacement of an excitation starting on the middle pigment ($\text{Tr}[\rho \hat{X}^2]$). For $V = 50 \text{ cm}^{-1}$, $N_{\text{traj}} = 10^4$; for $V = 100 \text{ cm}^{-1}$, $N_{\text{traj}} = 5 \times 10^3$. Parameters: $\lambda = \gamma = 50 \text{ cm}^{-1}$, $T = 295 \text{ K}$, $k_{\max} = 10$, and $\delta = 3 \times 10^{-4}$	31
4.1	LH2 monomer. (a) Side view: the B850 ring (18 BChl) and the B800 ring (9 BChl) are shown in green and blue, respectively. (b) Top view.	33
4.2	LH2 monomer. (a) The distance from equilibrium as a function of time (black) compared to a bi-exponential fit (green). Inset: Boltzmann distribution (green line) compared to adHOPS equilibrium populations (grey squares) of eigenstates ordered by absolute index ($ \nu $). (b) Population dynamics of the first seven eigenstates.	34
4.3	Exciton transport in a mesoscale aggregate of LH2. (a) LH2 37-mer. (b) adHOPS population dynamics of the donor and three concentric shells of B850 rings, color-coded to match panel a (c) Mean-squared deviation (MSD) of the excitation.	35
4.4	Exciton transport in a mesoscale aggregate of LH2. (a) Top: LH2 37-mer. Bottom: Schematic of a hexagonally-packed B850 complex with three concentric shells. Solid arrows represent the length scale of coherent transport; dashed arrows represent the onset of diffusive transport. (b) Diffusive late-time exciton transport (c) Coherent early-time exciton transport.	37
4.5	Population transport calculated with adHOPS (solid lines) and a single-exponential fit starting at 600 fs (dashed lines) in an LH2 dimer with inter-ring separation $R = 6.5 \text{ nm}$ (inset).	38

4.6	B850 dimer. (a) The dipole moments of the eigenstates of an LH2 monomer over 10^4 realizations of static disorder. (b) Transport rates for an LH2 dimer with an inter-ring separation of R when all couplings are allowed (circles) and when inter-ring couplings involving dark states are forbidden (squares).....	40
-----	--	----

LIST OF TABLES

Table	Page
4.1 LH2 exciton diffusion lengths in a hexagonally-packed lattice	39

CHAPTER 1

Introduction

The theoretical study of exciton transport in large molecular materials is limited by the computational efficiency of quantum dynamical algorithms. Excited state processes in molecular materials can occur after incident light excites a molecule. These processes are essential for the conversion of solar energy into current in artificial photosynthetic materials and organic semiconductors. However, most theoretical tools are not able to simulate these processes beyond a few pigments due to the exponential scaling of quantum dynamical algorithms.

Our starting point is a brief description of closed and open quantum systems. We then introduce non-Markovian systems and use that as a bridge to the Hierarchy of Pure States. The main goal of this thesis is to present a new method for solving open quantum systems which is both formally exact and computationally efficient for large systems.

1.1. Closed Quantum Systems

The fundamental modeling of quantum systems begins with a closed system. In closed quantum systems the system does not exchange any energy with its surroundings, effectively being isolated from any external stimuli. If the system is in a pure state we can model the dynamics using the Schrödinger equation

$$i\hbar \frac{\partial}{\partial t} |\psi(t)\rangle = \hat{H} |\psi(t)\rangle \quad (1.1)$$

where i is $\sqrt{-1}$, \hbar is the planks constant divided by 2π , $|\psi(t)\rangle$ is the time dependent wave function, and \hat{H} is the Hamiltonian for a closed system. Furthermore, since energy is conserved in a closed system the time evolution of the dynamics are unitary.

In the Schrödinger equation we have explicitly written the wave function as a state vector which is a convenient representation when we can write the states of the system as a linear combination of basis states. However, a state vector can only represent a pure state and many times the quantum system we are trying to describe cannot be described by a pure state. It is instead described by a mixed state, we can use ensembles, or statistical distributions of pure states, in order to fully characterize the quantum system. When the system is a mixed state the density operator formalism is useful. The density matrix can be thought of as similar to a wave function $|\psi\rangle$ and indeed any ensemble averaged value that the wave function can provide about the system the density matrix can also tell you. [1] The density matrix is given by,

$$\rho = \sum_i p_i |\psi_i\rangle \langle \psi_i| \quad (1.2)$$

where $|\psi_i\rangle$ is the wave function and p_i is the probability of finding the system in state $|\psi_i\rangle$ and is subject to the following constraints $p_i \geq 0$ and $\sum_i p_i = 1$ which is the normalization condition. The off diagonal elements are called the coherences. Coherences are complexed value correlations which relate the phase between states. In a closed quantum system the coherences are preserved but in an open quantum system the coherences can be lost due to the interaction the system and the environment.

For a closed quantum system the probability of being in a state p_i is time independent and we can time evolve a pure state or a mixed state regardless. The state vector $|\psi_i\rangle$ evolves

according to the Schrödinger equation. The resulting density matrix has the usual form

$$\rho_t = \sum_i p_i |\psi_i(t)\rangle \langle \psi_i(t)|. \quad (1.3)$$

Similarly to the Schrödinger equation of motion for a single state vector the density matrix equation of motion is given by,

$$\frac{d}{dt} \rho(t) = -\frac{i}{\hbar} [\hat{H}, \rho(t)]. \quad (1.4)$$

The equation above is what is known as the Liouville von-Nuemann equation (or the quantum Liouville equation). [1]

1.2. Open Quantum Systems

In reality no system is isolated from its environment and we call such systems open quantum systems. In open quantum systems the system is allowed to exchange energy with its surroundings and energy can be dissipated from the system. In other words, the system and its environment are coupled such that a change in one can affect the other. The total system now consist of the previously isolated quantum system in addition to an external environment. The total Hamiltonian is now a sum of three components,

$$\hat{H} = \hat{H}_S + \hat{H}_B + \hat{H}_{int} \quad (1.5)$$

where \hat{H}_S is the system Hamiltonian, \hat{H}_B is the bath Hamiltonian, and \hat{H}_{int} is the interaction Hamiltonian.

1.3. Hamiltonian's

1.3.1. System Hamiltonian

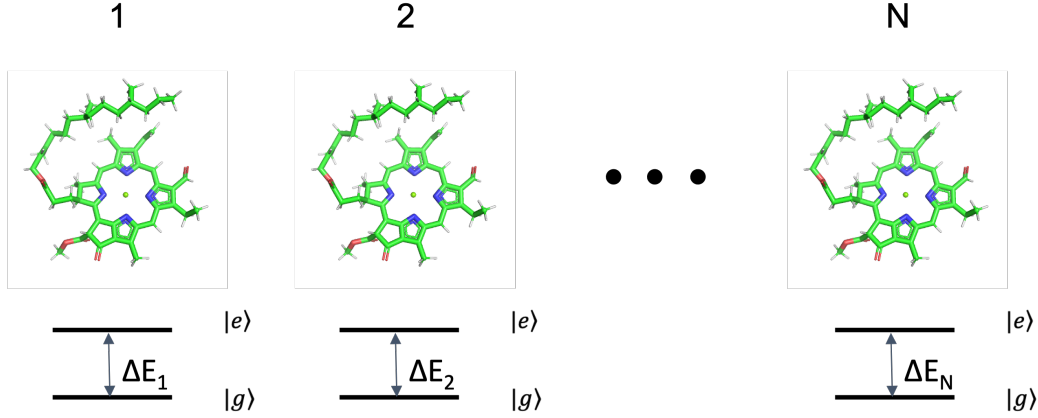


Figure 1.1: Schematic view of individual pigments in a linear chain

For the type of materials of interest in this thesis, such as organic semiconductors, photosynthetic complexes, and molecular crystals our electronic system is approximated as N monomers. As seen in Fig. 1.1 each pigment in the aggregate has 2 adiabatic electronic states, a ground state $|g\rangle$ and an excited state $|e\rangle$. The basis for our system Hamiltonian is compromised of the diabatic electronic basis of local states. The specific type of excitation used in this thesis is the Frenkel exciton [2], which are electrically neutral electron-hole pairs residing on the same molecule. The Frenkel exciton model neglects any charge transfer states arising from large electron-hole separation. The excitons are able to interact via the Coulomb potential. The Hamiltonian is given by,

$$\hat{H}_S = \sum_n |n\rangle E_n \langle n| + \sum_{n \neq m} |n\rangle V_{n,m} \langle m| \quad (1.6)$$

where, $|n\rangle$ are the pigments in the electronic system, E_n are the vertical excitation energies or the pigment energies, and $V_{n,m}$ are the electronic couplings between pigments. [3] The vertical excitation energies are the energy difference between the ground and first excited

state. The energy gap between the ground and excited state varies across time as the electronic system interacts with the solvent surrounding it. The electronic couplings are the interactions pigments feel from other pigments when in an aggregate allowing the transfer of energy between pigments.

1.3.2. Bath Hamiltonian

The bath Hamiltonian describes the thermal environment surrounding the system. The bath has the affect of introducing damping into the time-evolution of the system. The damping captures the fluctuations in the vertical excitation energies brought upon by the vibrations of the thermal environment. The classical analogue to the thermal environment is stochastic Brownian motion where a frictional force randomly acts to disturb the dynamics. All of the vibrational degrees of freedom are combined into a single bath that is coupled to the electronic degrees of freedom. In this thesis we describe the environment as a infinite set of coupled harmonic oscillators which mimic a continuous vibrational spectrum

$$\hat{H}_B = \sum_{n,q} \hbar \omega_{q_n} (\hat{a}_{q_n}^\dagger \hat{a}_{q_n} + 1/2) \quad (1.7)$$

where ω_{q_n} is the frequency of a harmonic oscillator and $\hat{a}_{q_n}^\dagger \hat{a}_{q_n}$ are the corresponding creation and annihilation operators. [3] The environment is divided by separable baths indexed by n containing a spectrum of harmonic modes, indexed by q .

1.3.3. Interaction Hamiltonian

The interaction Hamiltonian describes the coupling between the electronic degrees of freedom and the vibrational degrees of freedom. In our system each pigment in the electronic system is coupled to an independent bath. We introduce a set of normal modes given by q_n which are identical for both the ground and excited states. The interation component is

written as

$$\hat{H}_{int} = \sum_{n,q_n} \kappa_{q_n} \hat{L}_n \hat{q}_n \quad (1.8)$$

where κ_{q_n} is a bi-linear coupling term and \hat{L}_n is an operator ($\hat{L}_n = |n\rangle\langle n|$) that couples the n^{th} pigment to its independent environment described by bath modes q_n . [3] Upon excitation by incident photons there is a coupling of the electronic degrees of freedom to the vibrational degrees of freedom. The bi-linear term arises from the displacement of the equilibrium geometry of the excited state harmonic oscillator compared to that of the ground state harmonic oscillator. To properly structure the bath we must parameterize it in such a way that it mimics the actual vibrations induced by the environment.

1.3.3.1. Correlation Function

The time dependence of the system-bath interaction is described by the correlation function,

$$C_n(t) = \frac{\hbar}{\pi} \int_0^\infty d\omega J_n(\omega) (\coth(\hbar\beta\omega/2) \cos(\omega t) - i \sin(\omega t)) \quad (1.9)$$

where J_n is the spectral density, ω is the vibrational frequency, and β is the inverse temperature. In other words the damping provided by the thermal environment is contained in correlation function. The specific amount of damping is controlled by the relevant spectral densities. The spectral density describes which vibrational frequencies are present in the fluctuations brought upon by the thermal environment. The spectrum of vibrational frequencies can be approximated with an analytical form. In this work we use the Drude-Lorentz spectral density to describe the thermal environment of each pigment in the electronic system

$$J_n(\omega) = 2\lambda_n \gamma_{0_n} \frac{\omega}{\omega^2 + \gamma_{0_n}^2} \quad (1.10)$$

where λ is the reorganization energy, ω is the vibrational frequency, and γ is reorganization timescale. The reorganization timescale is the time required for the thermal environment to return to a new equilibrium state after a disturbance and the reorganization energy is the magnitude of how far from equilibrium the disturbance shifts the system.

CHAPTER 2

Non-Markovian Systems

For classical Markov systems the current state of the system is the only state of the system which can influence the next state. Non-Markovian systems are systems where a disturbance in the thermal environment caused by the state of the system can influence the dynamics of the system at some later time. This affect can be known as "memory" affects as the system has a memory of previous interactions that influence later time dynamics. If we imagine the time evolution of an open quantum system have finite discrete steps there are broadly three scenarios which can occur. First the timescale of reorganization of the thermal environment is fast compared to the electronic relaxation of the system. From the perspective of the electronic system the thermal environment is essentially constant and thus not influencing the dynamics of the electronic system. The second scenario is when the electronic system and thermal environment have similar reorganization timescales. The last scenario is when the timescale of reorganization of the thermal environment is slow compared to the electronic relaxation of the system. The second and third scenario both have a similar outcomes in which the thermal environment has not reached equilibrium between time evolution steps and consequently the thermal environment has a significant impact on the dynamics of the electronic system. The systems which operate in the second and third scenario are non-Markovian systems and the role of the "memory" must be treated correctly for accurate modeling.

2.1. Non-Markovian Quantum State Diffusion

Non-Markovian quantum state diffusion (NMQSD) [4] is a formally exact framework for solving non-Markovian open quantum systems problems. The NMQSD equation comes

from a coherent state basis description of the vibrational degrees of freedom where the full wave function $|\Psi_t\rangle$ is compromised of the electronic and vibrational degrees of freedom. The stochastic wave functions given by NMQSD can be ensemble averaged in order to reproduce the reduced density matrix

$$\rho_S = \mathbb{E}[|\psi(t; z_{n,t})\rangle\langle\psi(t; z_{n,t})|] \quad (2.1)$$

where $z_{n,t}$ is a complex stochastic process that indexes the wave function. $z_{n,t}$ follows the following statistical properties $\mathbb{E}[z_{n,t}] = 0$, $\mathbb{E}[z_{n,t}z_{n,s}] = 0$, and $\mathbb{E}[z_{n,t}^*z_{n,s}] = \alpha_n(t-s)$. The equation of motion for independent stochastic wave functions in multiple independent thermal environments is given by,

$$\begin{aligned} \partial_t |\psi(t; z_{n,t})\rangle &= (-i\hat{H}_S + \sum_n \hat{L}_n z_{n,t}^*) |\psi(t; z_{n,t})\rangle \\ &\quad - \sum_n \hat{L}_n^\dagger \int_0^t ds C_n(t-s) \frac{\delta|\psi(t; z_{n,t})\rangle}{\delta z_{n,s}^*} \end{aligned} \quad (2.2)$$

where C_n is the correlation function, $z_{n,t}$ is a complex stochastic process with $\mathbb{E}[z_{n,t}] = 0$, $\mathbb{E}[z_{n,t}z_{n,s}] = 0$, $\mathbb{E}[z_{n,t}^*z_{n,s}] = C_n(t-s)$, and \mathbb{E} denotes an ensemble average. In NMQSD the influence of the thermal environment is modeled via the complex stochastic process. The first term of the NMQSD represents the dynamics of the system where it a closed system. The second term represents the random fluctuations that the thermal environment imposes on the system. The last term known as the memory integral represents the "memory" that the system must keep track of. Unfortunately, the memory integral contains a functional derivative which spans the entire history of the trajectory thus a straightforward solution is extremely difficult.

2.2. Hierarchy of Pure States

The hierarchy of pure states (HOPS) [5] ameliorates the problem in NMQSD by replacing the functional derivative with a new term called an "auxiliary" wave function. For the rest of the thesis I will drop the explicit dependence of $z_{n,t}$ for notational simplicity. The auxiliary wave function is given by,

$$\begin{aligned} |\psi_t^{(1)}\rangle &= \int_0^t ds C(t-s) \frac{\delta |\psi_t\rangle}{\delta z_s^*} \\ &= D_t \psi_t^{(0)}. \end{aligned} \tag{2.3}$$

We note to continue the derivation of HOPS we must be able to write the correlation function as being composed of a sum of exponents

$$C_n(t) = \sum_{j_n} g_{j_n} e^{-\gamma_{j_n} t/\hbar}. \tag{2.4}$$

However, we will assume that we have a singular correlation function with one mode given by

$$C(t) = g e^{-\gamma t/\hbar}. \tag{2.5}$$

Having defined the auxiliary wave function we can now substitute $|\psi_t^{(1)}\rangle$ in to the NMQSD equation (eq 2.2)

$$\partial_t |\psi_t^{(0)}\rangle = -i \hat{H}_S |\psi_t^{(0)}\rangle + \hat{L} z_t^* |\psi_t^{(0)}\rangle - \hat{L}^\dagger |\psi_t^{(1)}\rangle. \tag{2.6}$$

The time evolution of the auxiliary wave function can, in turn, be determined by the product rule:

$$\partial \psi_t^{(1)} = \partial(D_t \psi_t^{(0)}) = (\partial D_t) \psi_t^{(0)} + D_t(\partial \psi_t^{(0)}) \tag{2.7}$$

The first term $(\partial D_t)\psi_t^{(0)}$ can be rewritten as:

$$(\partial D_t)\psi_t^{(0)} = \int_0^t ds \dot{C}(t-s) \frac{\delta \psi_t^{(0)}}{\delta z_s^*} \quad (2.8)$$

and if we recall that our correlation is composed of a single exponent, we can rewrite it as

$$(\partial D_t)\psi_t^{(0)} = -\gamma D_t \psi_t^{(0)} \quad (2.9)$$

The second term can be rewritten by recalling that $\partial \psi_t^{(0)}$ is given by eq. 2.6, which results in:

$$D_t(\partial \psi_t^{(0)}) = -i\hat{H}_S D_t \psi_t^{(0)} + \hat{L} D_t z_t^* \psi_t^{(0)} - \hat{L}^\dagger D_t \psi_t^{(1)} \quad (2.10)$$

Combining these two results, we find the (not-yet-simplified) equation for the time evolution of the auxiliary wave function:

$$\begin{aligned} \partial_t \psi_t^{(1)} = & -\gamma D_t \psi_t^{(0)} - i\hat{H}_S D_t \psi_t^{(0)} \\ & + \hat{L} D_t z_t^* \psi_t^{(0)} - \hat{L}^\dagger D_t \psi_t^{(1)} \end{aligned} \quad (2.11)$$

To further simplify this result, we want to rewrite this expression in terms of the auxiliary wave functions. The first and second terms follow from the definition of $\psi_t^{(1)}$, given by eq. 2.3. The fourth term can be defined as a new auxiliary wave function $\psi_t^{(2)}$. The third term, however, require further consideration.

$$\begin{aligned} \partial_t \psi_t^{(1)} = & -\gamma \psi_t^{(1)} - i\hat{H}_S \psi_t^{(1)} \\ & + \hat{L} D_t z_t^* \psi_t^{(0)} - L^\dagger \psi_t^{(2)} \end{aligned} \quad (2.12)$$

To simplify the expression $L_n D_t^{(1)} z_t^* \psi_t^{(0)}$, we will make use of the commutator relation $[D_t, z_s^*] = C(t-s)$. The full equation for the first order auxiliary wave function can then be rewritten simply in terms of the auxiliary wave functions and the wave function indexed by

0 ($\psi_t^{(0)}$) which is referred to as the physical wave function

$$\begin{aligned}\partial_t \psi_t^{(1)} &= (-i\hat{H} - \gamma + \hat{L}z_t^*)\psi_t^{(1)} \\ &\quad + C(0)\hat{L}\psi_t^{(0)} - \hat{L}^\dagger\psi_t^{(2)}.\end{aligned}\tag{2.13}$$

Extending the above argument to higher orders and then generalizing the results gives the linear HOPS equation for a single mode

$$\begin{aligned}\partial_t \psi_t^{(k)} &= (-i\hat{H}_s - k\gamma + \hat{L}z_t^*)\psi_t^{(k)} \\ &\quad + kC(0)\hat{L}\psi_t^{(k-1)} - L^\dagger\psi_t^{(k+1)}\end{aligned}\tag{2.14}$$

We now consider the NMQSD in the presence of multiple independent baths:

$$\partial_t \psi_t = -i\hat{H}\psi_t + \sum_n \hat{L}_n z_{n,t}^* \psi_t - \sum_n \hat{L}_n^\dagger \int_0^t ds C_n(t-s) \frac{\delta \psi_t}{\delta z_{n,s}^*} \tag{2.15}$$

where the noise process $z_{n,t}$ obeys the rules set out above, as well as $\mathbb{E}[z_{n,t} z_{m,s}^*] = \delta_{n,m} C_m(t-s)$: that is, each bath is not correlated with the others. We define a hierarchy of vector-indexed auxiliary wave functions as

$$|\psi_t^{(\vec{e}_n)}\rangle = \int_0^t ds C_n(t-s) \frac{\delta |\psi_t^{(\vec{0})}\rangle}{\delta z_{n,s}^*} = \hat{D}_t^{(n)} |\psi_t^{(\vec{0})}\rangle. \tag{2.16}$$

and define in turn, keeping in mind that $[\hat{D}_t^{(n)}, \hat{D}_t^{(m)}] = 0$, for indexing vector $\vec{k} = \sum_n k_n \vec{e}_n$

$$|\psi_t^{(\vec{k})}\rangle = \Pi_n (\hat{D}_t^{(n)})^{k_n} |\psi_t^{(\vec{0})}\rangle \tag{2.17}$$

Before moving forward, however, we note that the set of C_n may always be expressed as complex exponentials such that $C_n(t) = g_n e^{-\gamma_n t/\hbar}$. Consider a set of independent baths n , each with site projection operator \hat{L}_n and correlation function of arbitrary form other than complex exponentials $C_n(t)$. Because complex exponentials form an overcomplete basis, we

may express $C_n(t) = \sum_{j_n} g_{j_n} e^{-\gamma_{j_n} t/\hbar}$, which is the same as having a larger set of independent baths, each defined by $C_{j_n} = g_{j_n} e^{-\gamma_{j_n} t/\hbar}$ and $\hat{L}_{j_n} = \hat{L}_n$. We re-index this arbitrary set of baths such that $C_n(t) = g_n e^{-\gamma_n t/\hbar}$. When this is the case,

$$\delta_t |\psi_t^{\vec{0}}\rangle = -i\hat{H}_S |\psi_t^{\vec{0}}\rangle + \sum_n \hat{L}_n z_{n,t}^* |\psi_t^{\vec{0}}\rangle - \sum_n \hat{L}_n^\dagger |\psi_t^{e_n}\rangle \quad (2.18)$$

and

$$\partial_t \psi_t^{e_m} = (\partial_t \hat{D}_t^{(m)}) \psi_t^{\vec{0}} + \hat{D}_t^{(m)} (\partial_t \psi_t^{\vec{0}}) \quad (2.19)$$

which, since $[\hat{D}_t^{(n)}, \hat{D}_t^{(m)}] = 0$ and all $C_n(t)$ are complex exponentials, is simply

$$\begin{aligned} \delta_t |\psi_t^{\vec{e}_m}\rangle &= -\gamma_m |\psi_t^{\vec{e}_m}\rangle - i\hat{H}_S |\psi_t^{\vec{e}_m}\rangle \\ &\quad + \sum_n \hat{L}_n \hat{D}_t^{(m)} z_{n,t}^* |\psi_t^{\vec{0}}\rangle \\ &\quad - \sum_n \hat{L}_n^\dagger |\psi_t^{\vec{e}_m + \vec{e}_n}\rangle. \end{aligned} \quad (2.20)$$

We will now use the fact that

$$[\hat{D}_t^{(m)}, z_{n,t}^*] = \delta_{n,m} C_n(0) \quad (2.21)$$

$$\hat{D}_t^{(m)} z_{n,t}^* = \delta_{n,m} C_n(0) + z_{n,t}^* \hat{D}_t^{(m)} \quad (2.22)$$

to simplify the third term

$$\sum_n \hat{L}_n \hat{D}_t^{(m)} z_{n,t}^* |\psi_t^{\vec{0}}\rangle = \sum_n \hat{L}_n z_{n,t}^* \hat{D}_t^{(m)} |\psi_t^{\vec{0}}\rangle + \hat{L}_n C_n(0) |\psi_t^{\vec{0}}\rangle. \quad (2.23)$$

The full equation is now given by,

$$\begin{aligned}\partial|\psi_t^{\vec{e}_m}\rangle &= (-i\hat{H}_S - \gamma_m + \sum_n \hat{L}_n z_{n,t}^*)|\psi_t^{\vec{e}_m}\rangle \\ &\quad + \sum_n \delta_{m,n} \hat{L}_n C_n(0))|\psi_t^{\vec{0}}\rangle \\ &\quad - \sum_n \hat{L}_n^\dagger |\psi_t^{\vec{e}_m + \vec{e}_n}\rangle.\end{aligned}\tag{2.24}$$

If we extend to a general auxiliary indexing, given by \vec{k} , we obtain the linear HOPS equation

$$\begin{aligned}\partial|\psi_t^{(\vec{k})}\rangle &= (-i\hat{H}_S - \vec{k} \cdot \vec{\gamma} + \sum_n \hat{L}_n z_{n,t}^*)|\psi_t^{(\vec{k})}\rangle \\ &\quad + \sum_n \hat{L}_n C_n(0))|\psi_t^{(\vec{k} - \vec{e}_n)}\rangle \\ &\quad - \sum_n \hat{L}_n^\dagger |\psi_t^{(\vec{k} + \vec{e}_n)}\rangle\end{aligned}\tag{2.25}$$

noting that \vec{g} is the vectorized list of g_n and $|\psi_t^{\vec{k}}\rangle = 0$ if \vec{k} has any negative elements. The auxiliary wave functions which formulate the hierarchy are formally infinite.

In the linear HOPS equation, the contribution of each wave function to the ensemble is determined by $\|\psi_t^{\vec{0}}\|$, and this value will for most trajectories go towards zero with increasing time and for rare trajectories will diverge to infinity (with the ensemble mean remaining 1). This results in poor convergence behavior with respect to the number of trajectories needed to describe an ensemble property. This can be ameliorated by using the non-linear HOPS equation [5], derived via a Girsanov transformation of our linear equation. [6]

$$\begin{aligned}\hbar \partial_t |\psi_t^{(\vec{k})}\rangle &= (-i\hat{H}_S - \vec{k} \cdot \vec{\gamma} + \sum_n \hat{L}_n (z_{n,t}^* + \xi_{n,t}))|\psi_t^{(\vec{k})}\rangle \\ &\quad + \sum_n \vec{k}[n] g_n \hat{L}_n |\psi_t^{(\vec{k} - \vec{e}_n)}\rangle \\ &\quad - \sum_n (\hat{L}_n^\dagger - \langle \hat{L}_n^\dagger \rangle_t) |\psi_t^{(\vec{k} + \vec{e}_n)}\rangle,\end{aligned}\tag{2.26}$$

where

$$\xi_{t,n} = \frac{1}{\hbar} \int_0^t ds C_n^*(t-s) \langle L_n^\dagger \rangle_s \quad (2.27)$$

is a memory term that causes a drift in the effective noise, and

$$\langle \hat{L}_n^\dagger \rangle_t = \frac{\langle \psi_t^{(\vec{0})} | \hat{L}_n^\dagger | \psi_t^{(\vec{0})} \rangle}{\langle \psi_t^{(\vec{0})} | \psi_t^{(\vec{0})} \rangle}. \quad (2.28)$$

HOPS, just like NMQSD, is a formally exact framework for solving the time evolution of open quantum systems. It is convenient to think of HOPS calculations as depending on two basis sets: the state basis (\mathbb{S}) and the auxiliary basis (\mathbb{A}). The complete state basis is a finite set of vectors that span the Hilbert space of the system, while the complete auxiliary basis is composed of an infinite set of auxiliary wave functions indexed by vectors \vec{k} . To construct a finite auxiliary basis, the infinite hierarchy must be truncated. Here, we employ the common "triangular truncation" condition which limits the auxiliary basis a finite depth k_{max} such that $(\{\vec{k} \in \mathbb{A} : \sum_i k[i] \leq k_{max}\})$, though other static hierarchy filtering schemes have been proposed. [7]. In this work we couple each state to an independent bath leading to an incredibly unfavorable scaling of the number of auxiliary wave functions included in the triangular truncation. The formal scaling is given by $\binom{N_{state} + k_{max}}{k_{max}}$ which gives an overall $\mathcal{O}(N_{state}^{k_{max}})$ scaling for large aggregates. While convergence as a function of k_{max} is guaranteed, the requisite number of auxiliary wave functions is often prohibitive. The intractable scaling of HOPS past a few simulated molecules makes the application of HOPS to large molecular aggregates unfeasible.

CHAPTER 3

Results

The Hierarchy of Pure States (HOPS) is a formally exact solution to the time evolution of open quantum systems however it is limited to simulations of a few pigments due to its rapid scaling of computational expense. The key realization to increasing computational efficiency within HOPS is to realize that the delocalization extent of exciton wave function can be suppressed by the thermal environment. Previously, Markovian quantum state diffusion calculations have leveraged the locality of the exciton to reduce computational complexity using both a moving basis [8,9] and an adaptive basis. [10] Both of these approaches, however, require the conservation of probability, which is violated in the HOPS equations because amplitude in the auxiliary wave functions can be created and destroyed.

In this chapter we begin by further extending the Hierarchy of Pure States (HOPS) equation to normalize the physical wave function and the hierarchy allowing for a standardized magnitude of the derivative term with increasing depth of the hierarchy. We follow up by talking about the locality of the physical wave function of HOPS and extend this concept in order to build a reduced basis set for adaptive HOPS (adHOPS) that allows for size invariant scaling for large enough molecular aggregates.

3.1. Normalized Nonlinear HOPS

The adaptive Hierarchy of Pure States ensures that the magnitude of the derivative elements for auxiliary wave functions have a consistent absolute scale across the hierarchy. We begin by normalizing the physical wave function by dividing all wave functions by the

norm of the physical wave function

$$|\phi_t^{(\vec{k})}\rangle = \frac{|\psi_t^{(\vec{k})}\rangle}{\sqrt{\langle\psi_t^{(\vec{0})}|\psi_t^{(\vec{0})}\rangle}}. \quad (3.1)$$

The derivative of $\phi_t^{(\vec{k})}$ is given by,

$$\begin{aligned} \frac{d|\phi_t^{(\vec{k})}\rangle}{dt} &= \frac{\frac{d}{dt}|\psi_t^{(\vec{k})}\rangle}{\sqrt{\langle\psi_t^{(\vec{0})}|\psi_t^{(\vec{0})}\rangle}} - \left(\frac{1}{2}\right)|\psi_t^{(\vec{k})}\rangle(\langle\psi_t^{(\vec{0})}|\psi_t^{(\vec{0})}\rangle)^{-\frac{3}{2}}\frac{d}{dt}[\langle\psi_t^{(\vec{0})}|\psi_t^{(\vec{0})}\rangle] \\ &= \frac{\frac{d}{dt}|\psi_t^{(\vec{k})}\rangle}{\sqrt{\langle\psi_t^{(\vec{0})}|\psi_t^{(\vec{0})}\rangle}} - |\phi_t^{(\vec{k})}\rangle\frac{\frac{d}{dt}[\langle\psi_t^{(\vec{0})}|\psi_t^{(\vec{0})}\rangle]}{2\langle\psi_t^{(\vec{0})}|\psi_t^{(\vec{0})}\rangle} \end{aligned} \quad (3.2)$$

where we have transformed $|\psi_t^{(\vec{0})}\rangle$ to $|\phi_t^{(\vec{k})}\rangle$ by dividing $|\psi_t^{(\vec{0})}\rangle/\sqrt{\langle\psi_t^{(\vec{0})}|\psi_t^{(\vec{0})}\rangle}$ in the second part of the last equation in eq 3.2. If we further expand

$$\begin{aligned} \frac{\frac{d}{dt}\langle\psi_t^{(\vec{0})}|\psi_t^{(\vec{0})}\rangle}{2\langle\psi_t^{(\vec{0})}|\psi_t^{(\vec{0})}\rangle} &= \frac{1}{2}\langle\frac{d\psi_t^{(\vec{0})}}{dt}|\psi_t^{(\vec{0})}\rangle + \langle\psi_t^{(\vec{0})}|\frac{d\psi_t^{(\vec{0})}}{dt}\rangle/\langle\psi_t^{(\vec{0})}|\psi_t^{(\vec{0})}\rangle \\ &= \langle\psi_t^{(\vec{0})}|[-i\hat{H}_S + \sum_n \xi_{t,n}\hat{L}_n]\psi_t^{(\vec{0})}\rangle - \sum_n (L_n^\dagger - \langle L^\dagger \rangle_{t,n})|\psi_t^{e_n}\rangle/2\langle\psi_t^{(\vec{0})}|\psi_t^{(\vec{0})}\rangle + c.c. \end{aligned} \quad (3.3)$$

we are able to divide split the resulting form into four parts.

1. The first term goes to zero

$$\frac{-i\langle\psi_t^{(\vec{0})}|\hat{H}_S|\psi_t^{(\vec{0})}\rangle}{2\langle\psi_t^{(\vec{0})}|\psi_t^{(\vec{0})}\rangle} + \frac{i\langle\psi_t^{(\vec{0})}|\hat{H}_S|\psi_t^{(\vec{0})}\rangle}{2\langle\psi_t^{(\vec{0})}|\psi_t^{(\vec{0})}\rangle} \quad (3.4)$$

2. The second term is given by,

$$\begin{aligned}
& \sum_n (z_{t,n}^* + \xi_{t,n}) \frac{\langle \psi_t^{(\vec{0})} | \hat{L}_n | \psi_t^{(\vec{0})} \rangle}{2 \langle \psi_t^{(\vec{0})} | \psi_t^{(\vec{0})} \rangle} + c.c. \\
&= \frac{1}{2} \sum_n (z_{t,n}^* + \xi_{t,n}) \left\langle \frac{\psi_t^{(\vec{0})}}{\sqrt{\langle \psi_t^{(\vec{0})} | \psi_t^{(\vec{0})} \rangle}} \middle| \hat{L}_n \middle| \frac{\psi_t^{(\vec{0})}}{\sqrt{\langle \psi_t^{(\vec{0})} | \psi_t^{(\vec{0})} \rangle}} \right\rangle + c.c. \\
&= \frac{1}{2} \sum_n (z_{t,n}^* + \xi_{t,n}) \langle \phi_t^{(\vec{0})} | \hat{L}_n | \phi_t^{(\vec{0})} \rangle + c.c. \\
&= \sum_n \langle \hat{L}_n \rangle_t Re[(z_{t,n}^* + \xi_{t,n})]
\end{aligned} \tag{3.5}$$

3. The third term is given by,

$$\begin{aligned}
& \sum_n \frac{\langle \psi_t^{(\vec{0})} | \hat{L}_N^\dagger | \psi_t^{(\vec{e}_n)} \rangle}{2 \langle \psi_t^{(\vec{0})} | \psi_t^{(\vec{0})} \rangle} + c.c. \\
&= \frac{1}{2} \sum_n \left\langle \frac{\psi_t^{(\vec{0})}}{\sqrt{\langle \psi_t^{(\vec{0})} | \psi_t^{(\vec{0})} \rangle}} \middle| \hat{L}_N^\dagger \middle| \frac{\psi_t^{(\vec{e}_n)}}{\sqrt{\langle \psi_t^{(\vec{0})} | \psi_t^{(\vec{0})} \rangle}} \right\rangle + c.c. \\
&= \frac{1}{2} \sum_n \langle \phi_t^{(\vec{0})} | \hat{L}_N^\dagger | \phi_t^{(\vec{e}_n)} \rangle + c.c. \\
&= \sum_n Re[\langle \phi_t^{(\vec{0})} | \hat{L}_N^\dagger | \phi_t^{(\vec{e}_n)} \rangle]
\end{aligned} \tag{3.6}$$

4. The fourth term is given by,

$$\begin{aligned}
& \sum_n \langle \hat{L}^\dagger \rangle_{t,n} \frac{\langle \psi_t^{(\vec{0})} | \psi_t^{(\vec{e}_n)} \rangle}{2 \langle \psi_t^{(\vec{0})} | \psi_t^{(\vec{0})} \rangle} + c.c. \\
&= \frac{1}{2} \sum_n \langle \hat{L}^\dagger \rangle_{t,n} \left\langle \frac{\psi_t^{(\vec{0})}}{\sqrt{\langle \psi_t^{(\vec{0})} | \psi_t^{(\vec{0})} \rangle}} \middle| \frac{\psi_t^{(\vec{e}_n)}}{\sqrt{\langle \psi_t^{(\vec{0})} | \psi_t^{(\vec{0})} \rangle}} \right\rangle + c.c. \\
&= \frac{1}{2} \sum_n \langle \hat{L}^\dagger \rangle_{t,n} \langle \phi_t^{(\vec{0})} | \phi_t^{(\vec{e}_n)} \rangle + c.c. \\
&= \sum_n \langle \hat{L}^\dagger \rangle_{t,n} Re[\langle \phi_t^{(\vec{0})} | \phi_t^{(\vec{e}_n)} \rangle]
\end{aligned} \tag{3.7}$$

Summing these together we get:

$$\Gamma_t = \sum_n \langle \hat{L}_n \rangle_t \text{Re}[\xi_{t,n}] - \sum_n \text{Re}[\langle \phi_t^{(0)} | \hat{L}_N^\dagger | \phi_t^{(\vec{e}_n)} \rangle] + \sum_n \langle \hat{L}_n^\dagger \rangle \text{Re}[\langle \phi_t^{(0)} | \phi_t^{(\vec{e}_n)} \rangle] \quad (3.8)$$

The resulting equation of motion, where during the time-evolution the physical wave function has a norm of 1 is given by,

$$\begin{aligned} \dot{\phi}_t^{(\vec{k})} &= (-i\hat{H}_S - \vec{k} \cdot \vec{\gamma} - \Gamma_t + \sum_n L_n(z_{n,t}^* + \tilde{\xi}_{t,n}) |\phi_t^{(\vec{k})}\rangle \\ &\quad + \sum_n \vec{k}[n] C_n(0) L_n |\phi_t^{(\vec{k}-\vec{e}_n)}\rangle - \sum_n (L_n^\dagger - \langle \hat{L}_n^\dagger \rangle_t) |\phi_t^{(\vec{k}+\vec{e}_n)}\rangle) \end{aligned} \quad (3.9)$$

We now introduce $\tilde{\phi}_t^{(\vec{k})}$ which re-normalizes the auxiliary wave functions in the hierarchy, such that their norm does not diverge with increasing depth.

$$\tilde{\phi}_t^{(\vec{k})} = \frac{\phi_t^{(\vec{k})}}{\prod_n \left(\frac{C_n(0)}{\gamma_n} \right)^{\vec{k}[n]}} \quad (3.10)$$

For ease of notation let

$$\eta^{(\vec{k})} = \left(\prod_n \left(\frac{C_n(0)}{\gamma_n} \right)^{\vec{k}[n]} \right)^{-1}. \quad (3.11)$$

Just as before we take the derivative of $\tilde{\phi}_t^{(\vec{k})}$

$$\frac{d\tilde{\phi}_t^{(\vec{k})}}{dt} = \frac{d\phi_t^{(\vec{k})}}{dt} \eta^{(\vec{k})} \quad (3.12)$$

Since the additional correction factor is a constant with respect to time, it does not interact with the time-derivative and can be rewritten as:

$$\begin{aligned} \frac{d\tilde{\phi}_t^{(\vec{k})}}{dt} = & (-iH - \vec{k} \cdot \vec{\gamma} - \Gamma_0 + \sum_n \hat{L}_n(z_{t,n}^* + \tilde{\xi}_{t,n}) \phi_t^{(\vec{k})} \eta^{(\vec{k})} \\ & + \sum_n \vec{k}[n] C_n(0) \hat{L}_n \phi_t^{(\vec{k}-\vec{e}_n)} \eta^{(\vec{k})} \\ & - \sum_n (\hat{L}_n^\dagger - \langle L_n^\dagger \rangle_t) \phi_t^{(\vec{k}+\vec{e}_n)} \eta^{(\vec{k})} \end{aligned} \quad (3.13)$$

We can split eq. 3.13 into three parts. The first correspond to the self-interaction ('k-to-k') term:

$$\begin{aligned} &= \left(-iH - \vec{k} \cdot \vec{\gamma} - \Gamma_0 + \sum_N \hat{L}_n(z_{t,n}^* + \tilde{\xi}_{t,n}) \right) \phi_t^{(\vec{k})} \eta^{(\vec{k})} \\ &= \left(-iH - \vec{k} \cdot \vec{\gamma} - \Gamma_0 + \sum_n \hat{L}_n(z_{t,n}^* + \tilde{\xi}_{t,n}) \right) \tilde{\phi}_t^{(\vec{k})}. \end{aligned} \quad (3.14)$$

The second part $\vec{k} - e_n$ corresponds to the minus one term:

$$\begin{aligned} &= \sum_n \vec{k}[n] C_n(0) \hat{L}_n \phi_t^{(\vec{k}-\vec{e}_n)} \eta^{(\vec{k})} \\ &= \sum_n \vec{k}[n] C_n(0) \hat{L}_n \left(\frac{C_n(0)}{\gamma_n} \right)^{-1} \phi_t^{(\vec{k}-\vec{e}_n)} \eta^{(\vec{k}-\vec{e}_n)} \\ &= \sum_n \vec{k}[n] \gamma_n \hat{L}_n \tilde{\phi}_t^{(\vec{k}-\vec{e}_n)} \end{aligned} \quad (3.15)$$

Finally, the last part $\vec{k} + e_n$ corresponds to the plus one term:

$$\begin{aligned}
&= - \sum_n (\hat{L}_n^\dagger - \langle \hat{L}_n^\dagger \rangle_t) \phi_t^{(\vec{k} + \vec{e}_n)} \eta^{(\vec{k})} \\
&= - \sum_n \left(\frac{C_n(0)}{\gamma_n} \right) \left(\frac{\gamma_n}{C_n(0)} \right) (\hat{L}_n^\dagger - \langle \hat{L}_n^\dagger \rangle_t) \phi_t^{(\vec{k} + \vec{e}_n)} \eta^{(\vec{k})} \\
&= - \sum_n \left(\frac{C_n(0)}{\gamma_n} \right) (\hat{L}_n^\dagger - \langle \hat{L}_n^\dagger \rangle_t) \phi_t^{(\vec{k} + \vec{e}_n)} \eta^{(\vec{k})} \left(\frac{\gamma_n}{C_n(0)} \right) \\
&= - \sum_n \left(\frac{C_n(0)}{\gamma_n} \right) (\hat{L}_n^\dagger - \langle \hat{L}_n^\dagger \rangle_t) \phi_t^{(\vec{k} + \vec{e}_n)} \eta^{(\vec{k} + \vec{e}_n)} \\
&= - \sum_n \left(\frac{C_n(0)}{\gamma_n} \right) (\hat{L}_n^\dagger - \langle \hat{L}_n^\dagger \rangle_t) \tilde{\phi}_t^{(\vec{k} + \vec{e}_n)}. \tag{3.16}
\end{aligned}$$

The addition of the normalization of the hierarchy leads to the normalized non-linear HOPS equation

$$\begin{aligned}
\frac{d\tilde{\phi}_t^{(\vec{k})}}{dt} &= (-iH - \vec{k} \cdot \vec{\gamma} - \Gamma_t + \sum_n L_n(z_{n,t}^* + \tilde{\xi}_{t,n}) |\tilde{\phi}_t^{(\vec{k})}\rangle \\
&\quad + \sum_n \vec{k}[n] \gamma_n \hat{L}_n |\tilde{\phi}_t^{(\vec{k}-\vec{e}_n)}\rangle \\
&\quad - \sum_n \left(\frac{C_n(0)}{\gamma_n} \right) \cdot (\hat{L}_n^\dagger - \langle \hat{L}_n^\dagger \rangle_t) |\tilde{\phi}_t^{(\vec{k}+\vec{e}_n)}\rangle \tag{3.17}
\end{aligned}$$

where

$$\tilde{\xi}_{n,t} = \sum_n \frac{1}{\hbar} \int_0^t ds C_n^*(t-s) \langle \hat{L}_n^\dagger \rangle_t \tag{3.18}$$

and

$$\begin{aligned}
\Gamma_t &= \sum_n \langle \hat{L}_n \rangle_t \operatorname{Re}[z_{n,t}^* + \xi_{t,n}] \\
&\quad - \sum_n \left(\frac{C_n(0)}{\gamma_n} \right) \operatorname{Re}[\langle \tilde{\phi}_t^0 | \hat{L}_n^\dagger | \tilde{\phi}_t^{\vec{e}_n} \rangle] \\
&\quad + \sum_n \left(\frac{C_n(0)}{\gamma_n} \right) \langle \hat{L}_n^\dagger \rangle_t \operatorname{Re}[\langle \tilde{\phi}_t^0 | \tilde{\phi}_t^{\vec{e}_n} \rangle] \tag{3.19}
\end{aligned}$$

ensures normalization of the physical wave function.

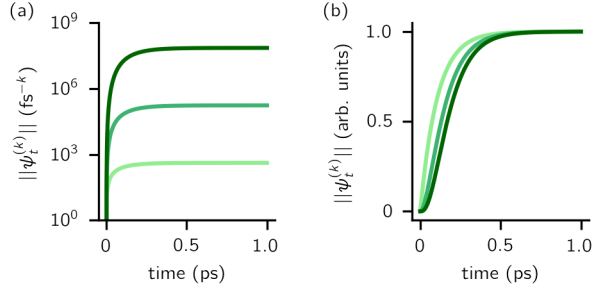


Figure 3.1: Magnitude of the first three auxiliaries in a single-mode HOPS calculation.
(a) The magnitude of the auxiliaries calculated using the non-linear HOPS equation (darker lines correspond to higher k values). (b) The magnitude of the auxiliaries calculated using the non-linear HOPS equation with the k -dependent prefactor

Without the additional terms to HOPS there is a divergent behavior in the magnitude of the auxiliary wave functions shown in Fig. 3.1(a). The divergent behavior shown in (a) is remedied by $\tilde{\phi}_t^{(\vec{k})}$. Figure 3.1(b) shows the result of the normalization of the hierarchy leading to an equal maximum magnitude for all auxiliaries.

3.2. Locality in HOPS

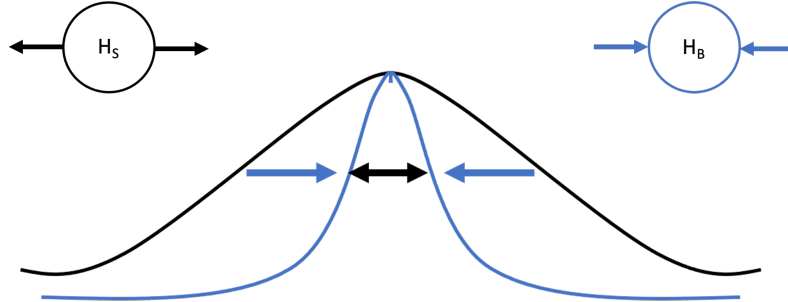


Figure 3.2: Dynamic localization induced by coupling to the environment

Within the quantum state diffusion formalism, stochastic wave functions localize in the presence of thermal environments. [8, 11, 12] To further expand on this, we look at our Hamiltonian for an open quantum system which has electronic and vibrational degrees of freedom coupled together. The electronic coupling in the system Hamiltonian serves to delocalize any excitation over the pigments (black curve in 3.2). On the other hand, the coupling to the vibrational degrees of freedom suppresses and localizes the wave function

(blue line in 3.2). The two reach an equilibrium at some point and in most materials the delocalization length does not exceed the 10s of pigments. [13–15]

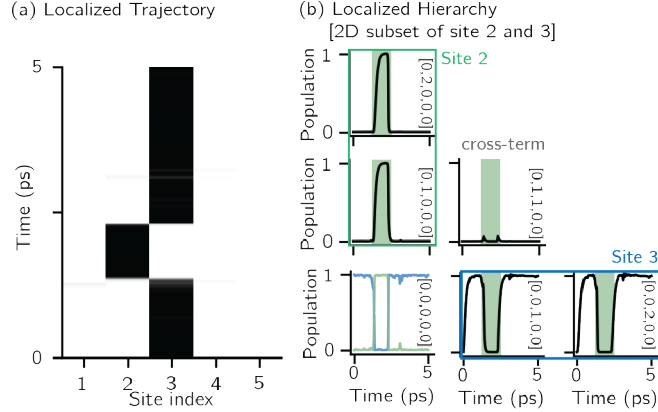


Figure 3.3: Localization in a single HOPS trajectory.(a) Contour map of site populations in the physical wave function (darker is more populated). (b) Norm-squared of auxiliary wave functions for a two-dimensional subset of the hierarchy associated with site 2 (column) and 3 (row). Panels are labelled by their index vector (\vec{k}). The shaded region represents the time-period when site 2 is occupied. The physical wave function ($\vec{k} = 0$) shows the populations of site 2 and 3 as green and blue lines, respectively. Parameters: $V = 10 \text{ cm}^{-1}$, $\lambda = \gamma = 50 \text{ cm}^{-1}$, $T = 295 \text{ K}$, and $k_{max} = 10$.

The same type of dynamic localization shows up in the HOPS wave functions. Fig. 3.3(a) shows a contour map of the time evolution of the physical wave function. The wave function is primarily localized on site 3, of a five site chain, for roughly the first 2 ps at which point it switches to primarily being localized on site 2. After roughly 0.5 ps the wave function localizes back on site 3 for the rest of the time evolution. In Fig. 3.3(b) we see a two dimensional subset of the hierarchy which corresponds to sites 2 and 3. The dynamics for site 2 and 3 of panel (a) are plotted in the bottom left hand plot. All other plots in Fig. 3.3(b) show the norm of the auxiliary wave functions. It is evident that there is a direct relationship between the population of the physical wave function and the magnitude of the norm for the auxiliary wave functions. The magnitude of the norm for site 3 is only 1 when the wave function is localized on site 3. When there is a switch to site 2 the auxiliaries associated with site 3 lose magnitude and the auxiliaries associated with site 2 gain magnitude. It is now evident how localization in the physical wave function induces localization in the hierarchy. We can

leverage the fact that the norms of specific auxiliary wave function are only populated when the physical wave function is localized in order to build a reduced basis set.

3.3. Adaptive Algorithm

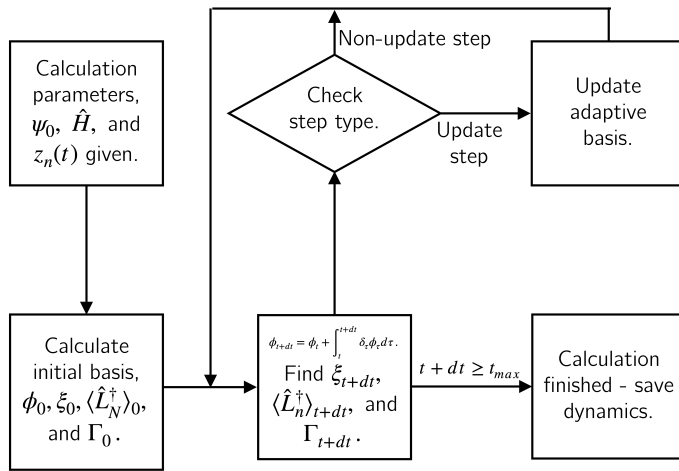
We have developed an adaptive algorithm for time-evolving the HOPS equations that leverages locality by constructing a reduced basis set at each time point that is still capable of describing the full dynamics. We establish the essential basis set elements at each time point (t) by ensuring that the error in the time-derivative introduced by the truncated auxiliary (\mathbb{A}_t) and state (\mathbb{S}_t) basis is below a given threshold (δ). We define the derivative error in terms of Euclidean distance between the true derivative vector and the effective derivative vector constructed using the adaptive basis. Because auxiliary wave functions share only nearest neighbor connections ($\vec{k} \pm \vec{e}_n \leftarrow \vec{k}$) and the Hamiltonian for a molecular aggregate supports electronic couplings over a finite spatial extent, the adaptive basis can be constructed with $\mathcal{O}(1)$ scaling. [16]

Our adHOPS algorithm neither assumes nor imposes locality. Rather, the adaptive basis takes advantage of whatever locality arises during the simulation. If the full hierarchy is required to satisfy the derivative error bound, adHOPS smoothly reverts to a HOPS calculation. As a result, adHOPS remains formally exact - the adaptive basis represents a time-dependent truncation of hierarchy elements, and δ , like k_{max} , is a convergence parameter. A visualization of the adHOPS algorithm is shown in Fig. 3.4 and a more detailed process is discussed below.

3.3.1. time-evolution

The adHOPS algorithm consists of repeated time integration of the HOPS equation given by eq. 3.17, broken up by updates to the adaptive basis. The algorithm begins with user inputted parameters such as the initial wave function and the Hamiltonian at which point

(a) The adHOPS algorithm



(b) The adaptive basis update algorithm

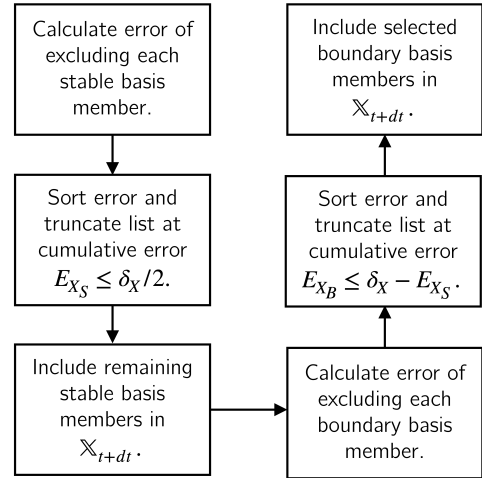


Figure 3.4: The adHOPS algorithm. (a) The overarching algorithm that an adaptive HOPS simulation follows. (b) The algorithm that updates the adaptive HOPS basis during update step

adHOPS will calculate the initial basis with $|\phi\rangle_t$ being the vector defining the full state of the system and bath, including all auxiliary wave functions in the current basis. The next step is to do a time-evolution step where, a sparse super-operator \hat{K}_t is defined such that $\hat{K}_t|\phi\rangle_t = \partial_t|\phi\rangle_t$. With this operator defined, we use fourth-order Runge-Kutta integration to calculate $|\phi\rangle_{t+dt} = |\phi\rangle_t + \int_t^{t+dt} \hat{K}_t|\phi\rangle_\tau d\tau$. At this point, quantities $\langle \hat{L}_n \rangle_{t+dt}$, $\xi_{n,t+dt}$, and Γ_{t+dt} are calculated based on eqs. (3.17-3.19) for use in the calculation of \hat{K}_{t+dt} . At this point adHOPS checks if the next time-evolution step is an update step or not. If it is the adaptive basis is updated in order to change what is in the basis. On the other hand, if it is not an update step then the Runge-Kutta is used again to update $|\phi\rangle_{t+dt}$. Once the time evolution is done the calculation is finished and the dynamics are accessible to save.

3.3.2. Basis Update Steps

When a time step is designated as an update step, adHOPS constructs a new basis set immediately after time-evolution. This process is detailed in Schema 3.4b. We can break down the basis construction into two steps: constructing the new auxiliary basis (\mathbb{A}_{t+dt}), introducing derivative error no greater than δ_A , and constructing the new state basis (\mathbb{S}_{t+dt}), introducing derivative error no greater than δ_S . When the direct sum basis is constructed, the order in which each basis is treated can influence the reduced basis. In our current adHOPS implementation we construct the new auxiliary basis before the new state basis.

The first step in constructing a new auxiliary basis is to calculate the derivative error associated with the exclusion of "stable" auxiliaries (elements in the current basis \mathbb{A}_t). The derivative error associated with removing a given auxiliary wave function is given by the L_2 norm of the resulting change in the derivative vector. The adaptive algorithm sorts this error from lowest to highest, and selects a cutoff point where the sum of the error is the maximum allowable error E_A (that is, the maximum possible error for which $E_A \leq \delta_A/2$). Finally, stable basis members beyond the cutoff point are included in \mathbb{A}_{t+dt} .

Next, the algorithm considers the derivative error associated with continuing to exclude the "boundary" auxiliaries. The algorithm sorts these elements from lowest to highest associated error, then includes elements in the basis up to a cutoff point such that the error associated with continuing to exclude the remaining boundary elements is the maximum allowable that is bounded by $\delta_A - E_A$.

Finally, this process is repeated for the state basis, with δ_S replacing δ_A . The derivative error associated with excluding a state basis element is given by the L_2 norm over the hierarchy basis \mathbb{A}_t : to avoid double-counting error associated with the exclusion of stable hierarchy elements, the stable hierarchy elements that have been filtered out during the

construction of \mathbb{A}_{t+dt} are ignored during the calculation of derivative error for excluding state basis members.

3.4. Adaptive Basis

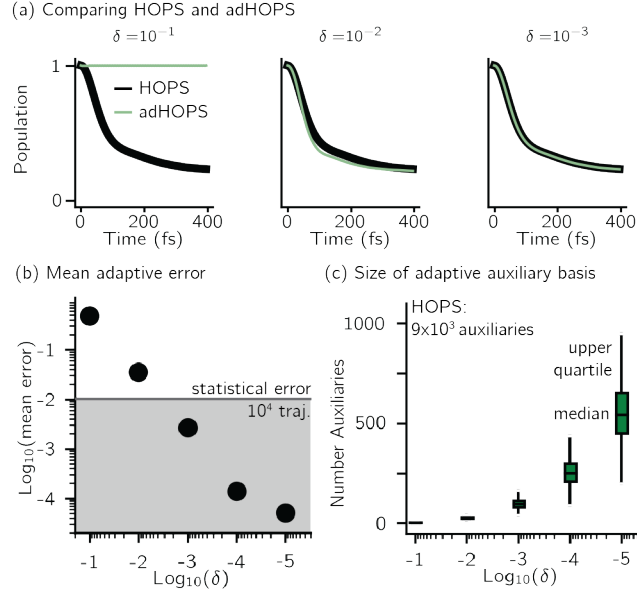


Figure 3.5: Comparing HOPS and adHOPS for a five-site linear chain. (a) Site 3 population dynamics for HOPS (black line) and adHOPS (green line). (b) Mean adaptive error as a function of δ . The grey region represents error beneath the statistical error for a 10^4 trajectory ensemble. (c) Ensemble distribution of the size of the adaptive auxiliary basis as a function of δ .

We use a simple five site chain in order to introduce the capabilities of adHOPS. In Fig. 3.5(a) the black lines are the HOPS dynamics while the green lines are adHOPS dynamics across different δ thresholds. When δ is large ($\delta = 0.1$) the allowed error is so large that the adaptive basis is discarding almost all of the auxiliaries and no exciton transport is realized. As we decrease the value of δ we see a better match to the HOPS dynamics. For the intermediate δ value ($\delta = 0.01$) there is only a small visible difference between HOPS and adHOPS. By the smallest δ value ($\delta = 0.001$) there is no distinguishable difference between HOPS and adHOPS. To further quantify the difference between HOPS and adHOPS Fig. 3.5(b) shows the mean adaptive error as a function of δ where in the gray region the adaptive error is smaller than the statistical error associated with the 10^4 trajectory ensemble.

By the time that we visually see no difference between HOPS and adHOPS the mean error is less than 10^{-2} and falls beneath the threshold of statistical error. Fig. 3.5(c) plots the ensemble distribution of the auxiliary basis size as a function of δ . For $\delta = 10^{-3}$, most adHOPS trajectories require 10^2 auxiliaries on average, or approximately 1% of the 9×10^3 auxiliaries required for a HOPS calculation.

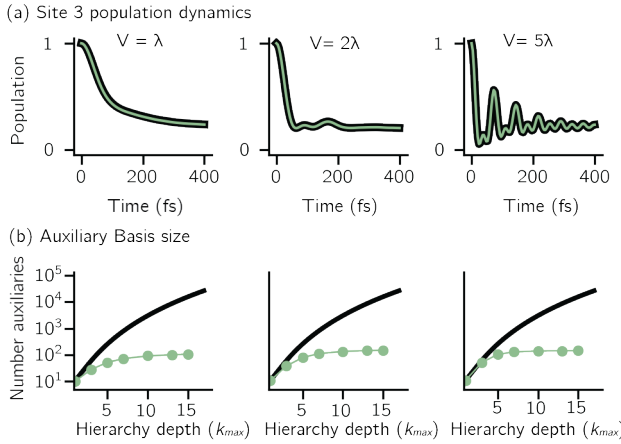


Figure 3.6: Comparing dynamics and auxiliary basis size as a function electronic coupling (V) for the full (black) and adaptive (green) HOPS calculations. (a) Site 3 population dynamics when $k_{max,10} = 10$. (b) Size of the auxiliary basis as a function of maximum hierarchy depth. Parameters: $V = 50 \text{ cm}^{-1}$, $\lambda = \gamma = 50 \text{ cm}^{-1}$, $T = 295 \text{ K}$, $k_{max} = 10$, and $N_{\text{traj}} = 10^4$.

Approximate methods depends on certain approximate conditions to be met. The ratio between the electronic coupling and the strength of the coupling to the environment is an important factor for some approximate methods. Forster relies on a weak electronic coupling between pigments while Refield relies on weak system bath coupling. Fig. 3.6(a) compares the full (black) and adaptive(green) HOPS dynamics with increasing electronic coupling (V). When we increase the electronic coupling the excitation can delocalize over a wider range of sites increasing the adaptive basis needed to accurately capture the dynamics. However, no matter the regime that we impose on adHOPS whether that be equal electronic coupling and reorganization energy or significantly greater electronic coupling we see that adHOPS always reproduces HOPS. Another way to increase the auxiliary basis is to increase k_{max} . Fig. 3.6(b) shows the corresponding size of the auxiliary basis as a function of k_{max} . Even

in the case of strong electronic coupling ($V = 5\lambda$) the adaptive auxiliary basis (green line) increases as a function of k_{max} much more slowly than the full HOPS auxiliary basis.

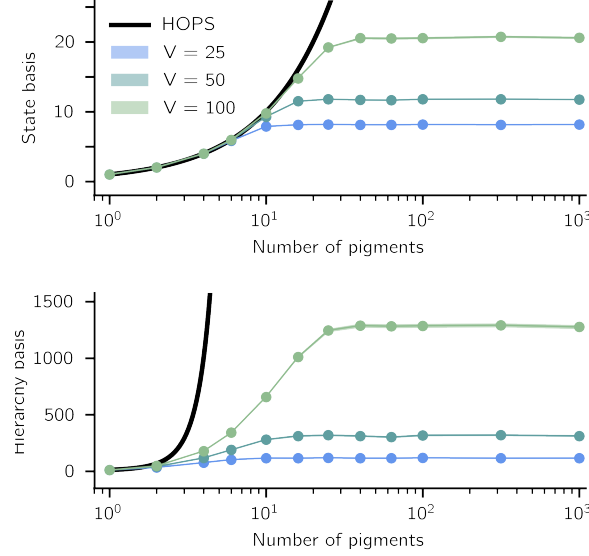


Figure 3.7: Advantageous scaling of adHOPS simulations for large numbers of pigments. Average number of elements in the adaptive system (top) and auxiliary (bottom) basis for linear chains of different lengths. Other parameters: $\lambda = \gamma = 50 \text{ cm}^{-1}$, $T = 295 \text{ K}$, $\delta = 10^{-3}$, and $N_{\text{traj}} = 10^4$. For $V = 250 \text{ cm}^{-1}$, $\gamma_{\text{mark}} = 1000 \text{ cm}^{-1}$, all others used $\gamma_{\text{mark}} = 500 \text{ cm}^{-1}$.

Another perpetual challenge for formally exact methods is their intractable computational scaling with the number of molecules. The scaling in HOPS calculations arises from the scaling of the auxiliary basis which is given by , whether you increases the size of the model system or the maximum depth of the hierarchy the auxiliary basis grows. Fig. 3.7(a) compares the full (black line) size of the state (top) and auxiliary (bottom) basis to the average size of the adaptive basis (colored lines) as a function of the number of molecules in a linear chain. The three colors, light blue, teal, and light green, represent different strengths of electronic coupling (V). A stronger electronic coupling leads to more delocalized states which in turn need a larger adaptive basis. Even when the electronic coupling is high we note that the size of the average auxiliary basis for adHOPS calculations increases much more slowly with the number of molecules than the full auxiliary basis. Moreover, both the

auxiliary and state bases in adHOPS calculations show a plateau beyond a threshold size of the linear chain ($N_{pig} > N^*$), indicating the onset of size invariant scaling. If we look back at section 3.2 we know that real systems do not delocalize to a large extent and when the material size gets much larger than the delocalization extent we expect the excitation to be spread out over a small fraction of the system. This result is exactly what drives the size invariant scaling of adHOPS. We find that adaptive calculations are faster than full calculations starting around $N_{pig} = 10$. Thus, for localized excitons, the size invariance of adHOPS allows for calculations on scales that were previously unachievable for formally exact methods.

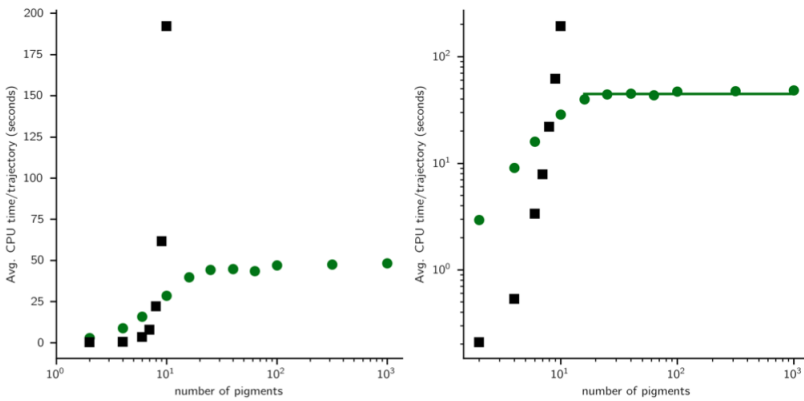


Figure 3.8: Average CPU time for HOPS (black squares) and adHOPS (green circles). The green line in the right panel shows a linear fit to the data from $N_{pig}=16$ to 1000, with a coefficient of 0.0277. Calculations were run using Intel Xeon 2.1 GHz processor.
 Parameters: $V = 50 \text{ cm}^{-1}$, $\lambda = \gamma = 50 \text{ cm}^{-1}$, $T = 295 \text{ K}$, $k_{max} = 10$, $\delta = 3 \times 10^{-4}$ and $N_{\text{traj}} = 10^4$.

In Fig. 3.8, we compare the CPU time required to run matched HOPS (black squares) and adHOPS (green circles) calculations. We measure the CPU time as the time required to propagate the equation-of-motion, excluding any time spent in the initial setup. HOPS calculations were only performed for $N_{pig} \leq 10$ due to the extreme computational expense for calculations of larger chains. We find that for small systems $N_{pig} \leq 10$ the overhead of computing the adaptive basis is more computationally costly than just running HOPS. However, starting at $N_{pig} = 10$, building the adaptive basis makes adHOPS calculations require less

CPU time per trajectory than the matched HOPS calculations. After $N_{pig} = 13$ the average CPU time for adHOPS calculations including up to 10^3 pigments reaches a plateau. Using the log-log plot for CPU time vs system size (Fig. 3.8, right panel) we determine a residual scaling of $\mathcal{O}(N_{pig}^{0.03})$ in the plateau region. We note that CPU time scales with the size of the basis, leading to greatly reduced simulation times for adaptive calculations. In other words, when using adHOPS increasing the number of pigments beyond a threshold size does not increase the computational expense of the calculation. Each adHOPS trajectory can be run on a single core making the calculations ‘embarrassingly’ (also called ‘perfectly’) parallel [17] as a result, HOPS ensembles can be computed using thousands of CPUs simultaneously without loss of efficiency.

adhOPS allows for calculations of ensemble properties on large molecular aggregates. A common experimental observable of interest is exciton diffusion however, it is difficult to calculate on long length scales. [18–20] Using adHOPS we are able to simulate exciton diffusion on a 10^3 linear chain with varying electronic coupling. Even with strong electronic coupling, adhOPS requires, on average, requires less than 2×10^3 auxiliary wave functions and 20 molecules in the state basis.

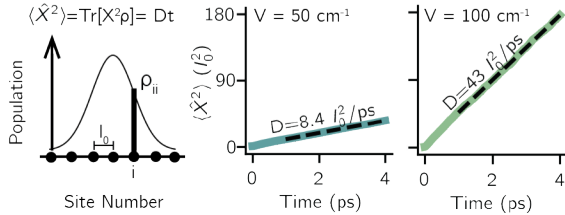


Figure 3.9: Exciton diffusion coefficient (in units of molecular spacing, l_0) for a 10^3 pigment chain from a linear fit to the mean-squared displacement of an excitation starting on the middle pigment ($\text{Tr}[\rho \hat{X}^2]$). For $V = 50 \text{ cm}^{-1}$, $N_{\text{traj}} = 10^4$; for $V = 100 \text{ cm}^{-1}$, $N_{\text{traj}} = 5 \times 10^3$. Parameters: $\lambda = \gamma = 50 \text{ cm}^{-1}$, $T = 295 \text{ K}$, $k_{\max} = 10$, and $\delta = 3 \times 10^{-4}$.

CHAPTER 4

Application

Photosynthesis is one of the most important biological processes on earth. The first step in photosynthesis is to capture light and efficiently shuttle it towards the reaction center where charge separation can occur allowing the process to continue. Photosynthetic organisms such as algae and plants have evolved specific light harvesting structures in order to complete this first crucial step. The faster the energy reaches the reaction center, the higher the photon-to-electron conversion efficiency. Recently, there has been an interest in using photosynthetic antenna complexes in bio-hybrid materials. [21–27]. Some of these bio-hybrid materials are packed far more densely than in natural systems in order to enhance exciton transport. Controlling exciton transport in artificial assemblies of light harvesting complexes requires understanding the mechanism of excitation transport on the nanoscale.

In this chapter we apply adHOPS to a light harvesting antenna complex in order to gain insights into the processes controlling excited state processes in bio-hybrid materials. We begin by outline our model system and then run calculations on the largest system to date ran with an exact equation of motion. Finally, we take a deeper dive into the mechanism that controls the diffusive transport in our model system.

4.1. Light Harvesting 2

Light harvesting complex 2 (LH2), is a well-studied system [28–31] that plays a major role as an antenna complex in the photosynthesis of purple bacteria and has previously been incorporated into artificial materials. [21, 22] The LH2 monomer (Fig. 4.1a-b) contains two rings of bacteriochlorophyll (BChl) that absorb at 800 nm (B800 ring, blue) and 850 nm

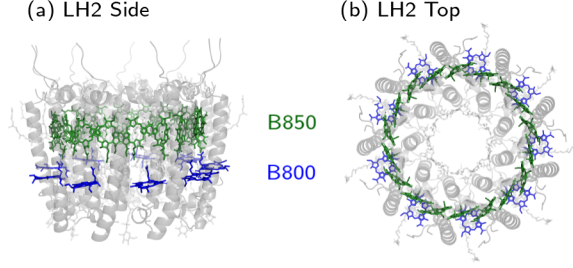


Figure 4.1: LH2 monomer. (a) Side view: the B850 ring (18 BChl) and the B800 ring (9 BChl) are shown in green and blue, respectively. (b) Top view.

(B850 ring, green), respectively. The B800 is comprised of 9 widely-spaced and weakly-coupled BChls. The primary purpose of B800 ring is to absorb light energy and funnel excitation to the B850 ring. The structure of the B850 ring consist of 18 tightly packed BChls split into $\alpha\beta$ pairs. The tight packing leads to 18 delocalized eigenstates which make up the eigenstate spectrum. The spectrum has 2 non-degenerate states $\nu = 0, 9$ and 8 pairs of degenerate states $\nu = \pm 1, \pm 2, \dots, \pm 8$. With the $\nu = \pm 1$ states being the optically bright states. The dimerized $\alpha\beta$ pairs give rise to a ninefold symmetry in the B850 ring. Since inter-LH2 transport occurs predominately between B850 rings, [32] we neglect the B800 pigments found in the 1NKZ pdb structure. [33] The ensemble is composed of an equal fraction of trajectories with excitations initiated in either the $\nu = 1$ or $\nu = -1$ eigenstate of the donor B850.

We model the Hamiltonian of the B850 ring using previously established parameters. [34] In the electronic ('system') Hamiltonian, the vertical excitation energies (or 'site energies') of the α and β chlorophylls are 12690 cm^{-1} and 12070 cm^{-1} , respectively, and the respective electronic couplings ($V_{n,m}$) within and between $\alpha\beta$ pairs are 307 cm^{-1} and 237 cm^{-1} . Following from ref [34] and section 1.3.3.1 we model the thermal environment of each pigment with a Drude-Lorentz spectral density characterized by a reorganization timescale ($\gamma_{0_n} = 53\text{ cm}^{-1}$) and reorganization energy ($\lambda_n = 65\text{ cm}^{-1}$). The corresponding correlation function is composed of one high temperature mode, k_{Mats} Matsubara modes, and an additional mode to ensure $\text{Im}[\alpha(0)] = 0$ (Appendix A). All other convergence parameters for this section

are given in the supplementary information of the corresponding paper "Formally Exact Simulations of Mesoscale Exciton Diffusion in a light Harvesting 2 Antenna Nanoarray". [35]

We employ two types of static disorder in our calculations: site energy static disorder and angular static disorder. Site energy static disorder accounts for random fluctuations in site energies stemming from movements of the protein structure on timescales longer than the simulation. The static disorder is introduced at the beginning of the simulation by shifting the diagonal entries of the system Hamiltonian (\hat{H}_S). These shifts in site energies are given by a real-valued Gaussian distribution of width σ centered on 0. In keeping with previous spectroscopic assignments, we also include static disorder on the site energy of each chlorophyll as Gaussian fluctuations with a standard deviation of $\sigma = 160 \text{ cm}^{-1}$. [31, 34] Angular static disorder accounts for the randomness of LH2 orientations inside of a membrane, and is represented by rotating the n th LH2 in a given aggregate by some angle θ_n about its nine-fold symmetric axis normal to the membrane. The values of θ_n were randomly selected from a uniform distribution.

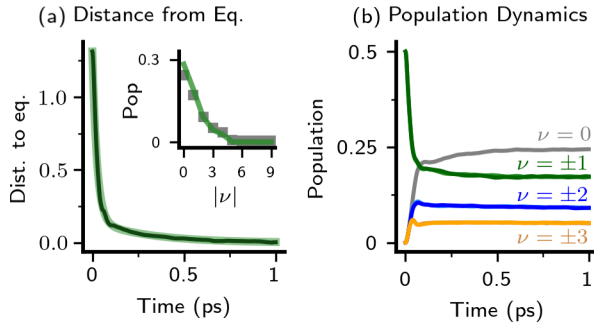


Figure 4.2: LH2 monomer. (a) The distance from equilibrium as a function of time (black) compared to a bi-exponential fit (green). Inset: Boltzmann distribution (green line) compared to adHOPS equilibrium populations (grey squares) of eigenstates ordered by absolute index ($|\nu|$). (b) Population dynamics of the first seven eigenstates.

Using adHOPS and our model of the B850 ring we capture the ultrafast relaxation of the bright state excitation to an equilibrium distribution. We characterize the relaxation of the exciton population towards equilibrium in a monomer using the 1-norm of a difference vector $\|\underline{P}(t) - \underline{P}_{eq}\|_1$ where $\underline{P}(t)$ and \underline{P}_{eq} are the eigenstate population vector of the B850

ring at time t and its equilibrium value, respectively. Using these parameters, the degenerate optically bright ($\nu = \pm 1$) states in the B850 ring relax to equilibrium on two timescales ($\tau_1 = 30$ fs and $\tau_2 = 300$ fs, Fig. 4.2a). The shortest and longest timescales of equilibration are associated with a rapid, quasi-coherent transport across eigenstates and a slow relaxation of population into the ground state, respectively (Fig. 4.2b). The timescales of relaxation calculated here are comparable to those found by global kinetic fits of B850 intraband relaxation in 2D electronic spectroscopy (50 fs and 150 fs), [36] though care should be taken with the comparison of relaxation between spectroscopic and population-based observables. At long time, the equilibrium eigenstate populations (Fig. 4.2a inset) form a Boltzmann distribution, slightly perturbed by the electron-vibrational coupling.

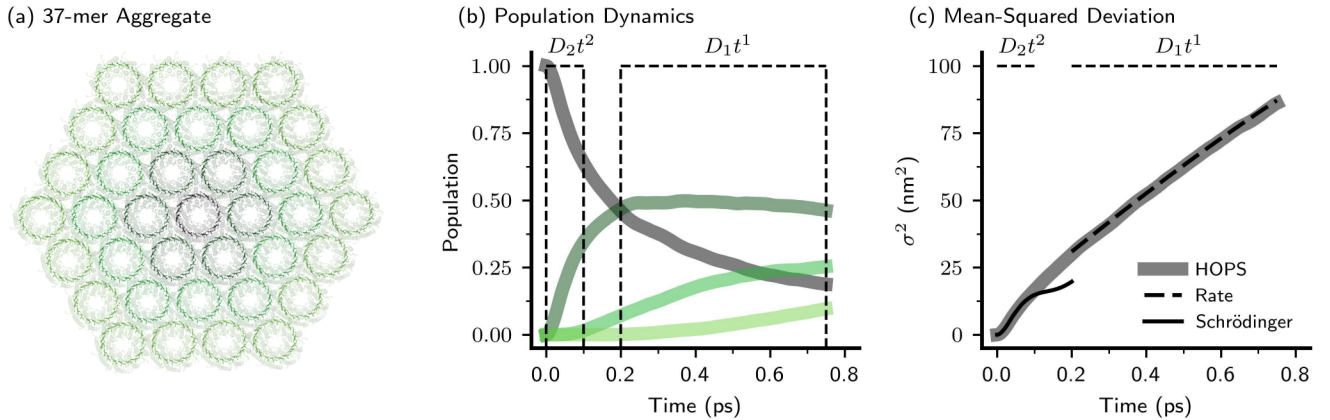


Figure 4.3: Exciton transport in a mesoscale aggregate of LH2. (a) LH2 37-mer. (b) adHOPS population dynamics of the donor and three concentric shells of B850 rings, color-coded to match panel a (c) Mean-squared deviation (MSD) of the excitation.

In order to investigate exciton diffusion in LH2 aggregates we construct a hexagonally-packed supercomplex containing 37 B850 rings (666 BChl) organized as three concentric shells around a donor ring (Fig. 4.3a) with center-to-center ring distances (R) of 6.5 nm. This inter-ring distance represents the closest packing of LH2 proteins proposed for artificial aggregates. [28, 37] While the parameters of each ring is established by a previous Hamilto-

nian, inter-ring couplings $\tilde{V}_{n,m}$ are calculated using the ideal dipole approximation

$$\tilde{V}_{n,m} = C \frac{\vec{d}_n \cdot \vec{d}_m - 3(\vec{d}_n \cdot \vec{r}_{n,m})(\vec{d}_m \cdot \vec{r}_{n,m})}{R_{n,m}^3} \quad (4.1)$$

where the coupling constant $C = 348,000 \text{ \AA}^3 \cdot \text{cm}^{-1}$, \vec{d}_n is a unit vector along the direction of the transition dipole moment of pigment n , and $\vec{r}_{n,m}$ ($R_{n,m}$) is the unit vector (distance) between Mg atoms in pigments n and m . Exciton transport between LH2 in the 37-mer has 2 distinct regimes an early and late time. Fig. 4.3b plots the excitation population calculated with adHOPS summed across the sequential concentric shells of LH2 acceptors. The first regime (narrow box in Fig. 4.3(b)), occurring on a sub 100 fs timescale is characterized by fast transport out of the center into the first concentric shell covering an area of $\sim 100 \text{ nm}^2$. The second regime, (wider box in Fig. 4.3b), excitation transport occurs is slower and the 2nd and 3rd concentric shells begins to populate. Fig. 4.3(c) shows the mean squared deviation (MSD) of the excitation. The MSD is given by,

$$MSD(t) = \sum_n P_n(t) R_{0n}^2 \quad (4.2)$$

where P_n is the population of the n^{th} B850 ring and $n = 0$ signifies the donor. The two timescales of exciton transport can be seen in the MSD, where on the first time scale there is a sharp increase in the MSD curve followed by a decrease post 200fs that is linear in time.

Fig 4.4 investigates the mechanisms of exciton transport in the 37-mer. The extremely fast rate of transport out of the center ring suggests a coherent mechanism. In Fig. 4.4(b) we compare the dynamics of our adHOPS ensemble to a coherent equation of motion that excludes the vibrational environment (i.e., the Schrödinger equation) while including both site energy and angular static disorder. On the sub 100 fs timescale the two methods reproduce each other, in both population dynamics as well as the MSD curve, and we can assign the first timescale to a purely coherent mechanism. Past 100 fs the purely coherent mechanism

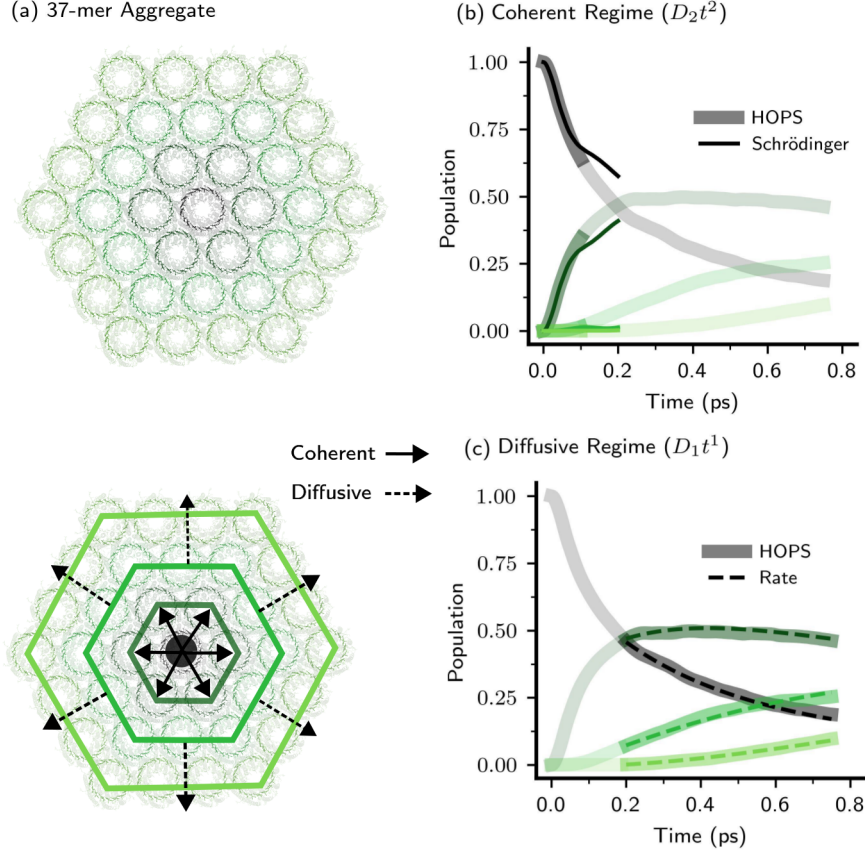


Figure 4.4: Exciton transport in a mesoscale aggregate of LH2. (a) Top: LH2 37-mer. Bottom: Schematic of a hexagonally-packed B850 complex with three concentric shells. Solid arrows represent the length scale of coherent transport; dashed arrows represent the onset of diffusive transport. (b) Diffusive late-time exciton transport (c) Coherent early-time exciton transport.

breaks down and no longer reproduces adHOPS population dynamics or the MSDS curve, which is consistent with the reorganization time characterizing the spectral density. For the second timescale, post 200 fs, the slower transport of excitation along with a linear MSD curve suggest an incoherent mechanism. In Fig. 4.4(c) we compare the adHOPS dynamics to a kinetic model. The model is described by

$$\dot{\underline{P}}(t) = \underline{\underline{K}} \underline{P}(t), \quad (4.3)$$

with a rate matrix (\underline{K}) that only connects nearest-neighbor rings via a symmetric transport rate κ . We find the average rate of transport calculated for an LH2 dimer ($\kappa_{\text{avg}} = 0.53 \pm 0.03 \text{ ps}^{-1}$) overestimates the long-time rate because of the early-time coherent dynamics. However, we can isolate an effective incoherent transport rate ($\kappa_{\text{dimer}} = 0.44 \pm 0.04 \text{ ps}^{-1}$) from the long-time dynamics between the donor and acceptor LH2 (dashed line, Fig. 4.5, which can be characterized by a single exponential. Given the correct exciton population at 200 fs, this kinetic model reproduces the the long-time dynamics of the concentric shell populations.

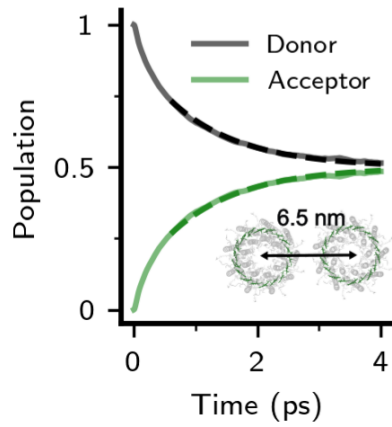


Figure 4.5: Population transport calculated with adHOPS (solid lines) and a single-exponential fit starting at 600 fs (dashed lines) in an LH2 dimer with inter-ring separation $R = 6.5 \text{ nm}$ (inset).

At this point, the mesoscale nature of the 37-mer becomes clear: it is the smallest aggregate sufficient to observe the turn over from the short-time coherent to long-time diffusive transport mechanisms and cannot be fully described by approximate methods limited to either regime. The early-time coherent mechanism can be characterized with a nearest-neighbor model composed of the donor ring and first concentric shell of acceptors. However, by the onset of diffusive transport (200 fs) the second concentric shell of B850 acceptor rings already contains nearly 10% of the exciton population. As a result, characterizing diffusive transport without edge effects requires a third concentric shell and an aggregate containing 37 LH2 and a total of 666 bacteriochlorophyll.

Table 4.1: LH2 exciton diffusion lengths in a hexagonally-packed lattice

R (nm)	D_1 (nm 2 /ps)	L_d (nm)
6.5	110 ± 10	330 ± 20
7.5	43 ± 3	210 ± 6
8.5	19 ± 1	140 ± 4

The uncertainty represents the 95%
confidence interval.

To characterize the diffusion extent of LH2 aggregates we use the kinetic model paired with an infinite aggregate to predict the diffusion length. Table 4.1 reports the excitation diffusion length in the kinetic model for three LH2 packing distances. The diffusion length is given by,

$$L_d^2 = 6R^2\kappa_{dimer}\tau \equiv D\tau, \quad (4.4)$$

where the factor of 6 arises from hexagonal packing, R is the packing distance, κ_{dimer} is the rate of transport between dimers, and τ is the lifetime of the exciton (assumed to be 1 ns). [38] At a biologically relevant inter-ring distance of $R = 8.5$ nm, our excitation diffusion length ($L_d = 140$ nm) is consistent with a previous order of magnitude estimate [39] and greatly exceeds that of boron sub-naphthalocyanine chloride (21 nm), fullerene (19 nm), and other prototypical organic semiconductors (< 30 nm). [40, 41] Moreover, our rate of transport at $R = 8.5$ nm is smaller than some previous estimates (e.g., 0.241 ps $^{-1}$ in Ref. [42]), suggesting other LH2 Hamiltonians proposed in the literature could support even longer excitation diffusion lengths.

Recently, a dark state shelving mechanism has been proposed to modulate transport in close-packed LH2 aggregates, [28] but we find that inter-ring transport is dominated by coupling between bright states. The bright states are commonly referred to as "bright" due to their ability to absorb light and fluoresce light making them optically bright. Dark states on the other hand, do not fluoresce light and thus are optically dark. Using the dipole moments of the eigenstate of B850, with 10^4 realizations of static disorder, (Fig. 4.6(a)) we classify

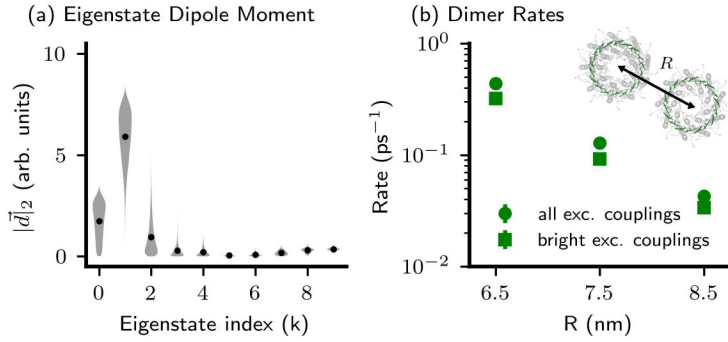


Figure 4.6: B850 dimer. (a) The dipole moments of the eigenstates of an LH2 monomer over 10^4 realizations of static disorder. (b) Transport rates for an LH2 dimer with an inter-ring separation of R when all couplings are allowed (circles) and when inter-ring couplings involving dark states are forbidden (squares).

the first three eigenstates as bright ($|\nu| \leq 2$) due to their large average dipole magnitude, and all other eigenstates ($|\nu| \leq 2$) are classified as dark states. Fig. 4.6(b) compares the rates of population transport with all eigenstates contributing to transport \hat{H}_S (circles) and with inter-ring couplings via the dark states removed (squares) at various center-to-center dimer separations R . Neglecting dark state dependent inter-ring transport reduces the long-time rate (κ_{dimer}) by 20 – 30% across the inter-ring separations (R) studied here. The recently, proposed dark state shelving mechanism relied on an exceptionally fast inter ring transport rate ($\kappa_{\text{dimer}} \geq 10 \text{ ps}^{-1}$ at $R=6.5 \text{ nm}$) predicted by their Lindblad calculations. The Lindblad calculations suggest inter-ring transport occurs before the intra-ring thermalization boosting the role of dark states. Additionally, The incoherent (i.e., diffusive) transport between B850 rings controlled by bright states reflects the previously proposed supertransfer mechanism in which delocalization around the B850 ring leads to enhanced exciton dipole moments and accelerated transport between rings. [43–47]

APPENDIX A

Matsubara Decomposition

The bath correlation function is described by a Drude-Lorentz spectral density $J_n(\omega)$ (eq.1.10), and is decomposed into a collection of exponential contributions

$$C_n(t) = \sum_{j_n} g_{j_n} e^{-\gamma_{j_n} t/\hbar}. \quad (1.1)$$

The specific values of g_{j_n} and γ_{j_n} are given by the Matsubara decomposition of the Drude-Lorentz spectral density:

$$g_{0_n} = 2\lambda_n \beta^{-1} \left(1 + \sum_{j_n=1}^{k_{Mats}} \frac{\gamma_{0_n}^2}{\gamma_{0_n}^2 - \gamma_{j_n}^2} \right) - i\lambda_n \gamma_{0_n} \quad (1.2)$$

for the "high-temperature" mode, and

$$g_{j_n} = \frac{2i}{\beta} J_n(i\gamma_{j_n}), \quad \gamma_{j_n} = \frac{2\pi j}{\beta} \quad (1.3)$$

for Matsubara modes $j \neq 0$, where k_{Mats} is the number of Matsubara modes included. To ensure that $C_n(-t) = C_n^*(t)$, we also include one other mode in each correlation function with a prefactor

$$g_{Mark_n} = i\lambda_n \gamma_{0_n} \quad (1.4)$$

and a decay timescale that matches the fastest-decaying Matsubara mode.

BIBLIOGRAPHY

- [1] D. J. Tannor, *Introduction to quantum mechanics a time dependent perspective*. University Science Books, 2006. 2, 3
- [2] J. Frenkel, *On the transformation of light into heat in solids. i*, *Phys. Rev.* **37** (Jan, 1931) 17–44. 4
- [3] O. Kühn, *Handbook of organic materials for electronic and photonic devices*. Wooodhead Publishing, 2019. 4, 5, 6
- [4] L. Diosi and W. T. Strunz, *The non-Markovian stochastic Schrodinger equation for open systems*, *Phys. Lett. A* **235** (1997) 569–573. 8
- [5] D. Suess, A. Eisfeld and W. T. Strunz, *Hierarchy of Stochastic Pure States for Open Quantum System Dynamics*, *Phys. Rev. Lett.* **113** (Oct., 2014) 150403. 10, 14
- [6] L. Diósi, N. Gisin and W. T. Strunz, *Non-markovian quantum state diffusion*, *Phys. Rev. A* **58** (Sep, 1998) 1699–1712. 14
- [7] P.-P. Zhang, C. D. B. Bentley and A. Eisfeld, *Flexible scheme to truncate the hierarchy of pure states*, *J. Chem. Phys.* **148** (2018) 134103. 15
- [8] R. Schack, T. A. Brun and I. C. Percival, *Quantum state diffusion, localization and computation*, *J. Phys. A Math. Gen.* **28** (Sept., 1995) 5401–5413. 16, 22
- [9] R. Schack, T. A. Brun and I. C. Percival, *Quantum-state diffusion with a moving basis: Computing quantum-optical spectra*, *Phys. Rev. A* **53** (Apr., 1996) 2694–2697. 16
- [10] X. Gao and A. Eisfeld, *Charge and energy transfer in large molecular assemblies: Quantum state diffusion with an adaptive basis*, *J. Chem. Phys.* **150** (June, 2019) 234115. 16
- [11] N. Gisin and I. C. Percival, *Quantum state diffusion, localization and quantum dispersion entropy*, *Journal of Physics A: Mathematical and General* **26** (May, 1993) 2233–2243. 22
- [12] N. Gisin and I. C. Percival, *The quantum state diffusion picture of physical processes*, *J. Phys. A Math. Gen.* **26** (May, 1993) 2245–2260. 22
- [13] D. I. G. B. Roden, Jan J. J. and K. B. Whaley., *Long-range energy transport in photosystem ii.*, *J. Chem. Phys.* **144** (2016) 14. 23
- [14] D. H. Arias, K. W. Stone, S. M. Vlaming, B. J. Walker, M. G. Bawendi, R. J. Silbey et al., *Thermally-limited exciton delocalization in superradiant molecular aggregates*, *J. Phys. Chem. B* **117** (2013) 4553–4559, [<https://doi.org/10.1021/jp3086717>]. 23

- [15] A. Ruseckas, P. Wood, I. D. W. Samuel, G. R. Webster, W. J. Mitchell, P. L. Burn et al., *Ultrafast depolarization of the fluorescence in a conjugated polymer*, *Phys. Rev. B* **72** (Sep, 2005) 115214. 23
- [16] L. Varvelo, J. K. Lynd and D. I. G. Bennett, *Formally exact simulations of mesoscale exciton dynamics in molecular materials*, *Chem. Sci.* **12** (2021) 9704–9711. 24
- [17] M. Herlihy, N. Shavit, V. Luchangco and M. Spear, *The art of multiprocessor programming*. Newnes, 2020. 31
- [18] S. K. Saikin, M. A. Shakirov, C. Kreisbeck, U. Peskin, Y. N. Proshin and A. Aspuru-Guzik, *On the long-range exciton transport in molecular systems: the application to H-aggregated heterotriangulene chains*, *J. Phys. Chem. C* **121** (Nov., 2017) 24994–25002. 31
- [19] M. Delor, A. H. Slavney, N. R. Wolf, M. R. Filip, J. B. Neaton, H. I. Karunadasa et al., *Carrier diffusion lengths exceeding 1 Mm despite trap-limited transport in halide double perovskites*, *ACS Energy Lett.* (Apr., 2020) 1337–1345. 31
- [20] Y. Wan, Z. Guo, T. Zhu, S. Yan, J. Johnson and L. Huang, *Cooperative singlet and triplet exciton transport in tetracene crystals visualized by ultrafast microscopy*, *Nat. Chem.* **7** (Oct., 2015) 785–792. 31
- [21] N. P. Reynolds, S. Janusz, M. Escalante-Marun, J. Timney, R. E. Ducker, J. D. Olsen et al., *Directed formation of micro- and nanoscale patterns of functional light-harvesting LH₂ complexes*, *J. Am. Chem. Soc.* **129** (2007) 14625–14631. 32
- [22] M. Escalante, P. Maury, C. M. Bruinink, K. van der Werf, J. D. Olsen, J. A. Timney et al., *Directed assembly of functional light harvesting antenna complexes onto chemically patterned surfaces*, *Nanotechnology* **19** (2007) 025101. 32
- [23] M. Escalante, Y. Zhao, M. J. W. Ludden, R. Vermeij, J. D. Olsen, E. Berenschot et al., *Nanometer arrays of functional light harvesting antenna complexes by nanoimprint lithography and hostguest interactions*, *J. Am. Chem. Soc.* **130** (2008) 8892–8893. 32
- [24] C. Vasilev, M. P. Johnson, E. Gonzales, L. Wang, A. V. Ruban, G. Montano et al., *Reversible switching between nonquenched and quenched states in nanoscale linear arrays of plant light-harvesting antenna complexes*, *Langmuir* **30** (2014) 8481–8490. 32
- [25] J. A. Mancini, G. Kodali, J. Jiang, K. R. Reddy, J. S. Lindsey, D. A. Bryant et al., *Multi-step excitation energy transfer engineered in genetic fusions of natural and synthetic light-harvesting proteins*, *J. R. Soc. Interface.* **14** (2017) 20160896. 32
- [26] T. Yoneda, Y. Tanimoto, D. Takagi and K. Morigaki, *Photosynthetic model membranes of natural plant thylakoid embedded in a patterned polymeric lipid bilayer*, *Langmuir* **36** (2020) 5863–5871. 32
- [27] Y. J. Kim, H. Hong, J. Yun, S. I. Kim, H. Y. Jung and W. Ryu, *Photosynthetic nanomaterial hybrids for bioelectricity and renewable energy systems*, *Adv. Mater.* **33** (2021) 2005919. 32
- [28] A. Mattioni, F. Caycedo-Soler, S. F. Huelga and M. B. Plenio, *Design principles for long-range energy transfer at room temperature*, *Phys. Rev. X* **11** (2021) 041003. 32, 35, 39

- [29] F. Zheng, L. Chen, J. Gao and Y. Zhao, *Fully quantum modeling of exciton diffusion in mesoscale light harvesting systems*, *Materials* **14** (2021) 3291. 32
- [30] J. Strümpfer and K. Schulten, *Light harvesting complex II b850 excitation dynamics*, *J. Chem. Phys.* **131** (2009) 225101. 32
- [31] G. D. Scholes and G. R. Fleming, *On the mechanism of light harvesting in photosynthetic purple bacteria: B800 to b850 energy transfer*, *J. Phys. Chem. B* **104** (2000) 1854–1868. 32, 34
- [32] X. Hu, T. Ritz, A. Damjanović, F. Autenrieth and K. Schulten, *Photosynthetic apparatus of purple bacteria*, *Q. Rev. Biophys.* **35** (2002) 1–62. 33
- [33] M. Z. Papiz, S. M. Prince, T. Howard, R. J. Cogdell and N. W. Isaacs, *The structure and thermal motion of the b800–850 lh2 complex from rps. acidophila at 2.0 Å resolution and 100k: New structural features and functionally relevant motions*, *J. Mol. Biol.* **326** (2003) 1523–1538. 33
- [34] C. Smyth, D. G. Oblinsky and G. D. Scholes, *B800–B850 coherence correlates with energy transfer rates in the LH2 complex of photosynthetic purple bacteria*, *Phys. Chem. Chem. Phys.* **17** (2015) 30805–30816. 33, 34
- [35] B. C. O. K. Leonel Varvelo, Jacob K. Lynd and D. I. G. B. Raccah, *Formally exact simulations of mesoscale exciton diffusion in a light-harvesting 2 antenna nanoarray*, *J. Phys. Chem. Lett.* **14** (Jan, 2023) 3077–2083. 34
- [36] E. Thyrhaug, M. Schröter, E. Bukartè, O. Kühn, R. Cogdell, J. Hauer et al., *Intraband dynamics and exciton trapping in the LH2 complex of Rhodopseudomonas acidophila*, *J. Chem. Phys.* **154** (2021) 045102. 35
- [37] M. Escalante, A. Lenferink, Y. Zhao, N. Tas, J. Huskens, C. N. Hunter et al., *Long-range energy propagation in nanometer arrays of light harvesting antenna complexes*, *Nano Lett.* **10** (2010) 1450–1457. 35
- [38] A. Freiberg, M. Rätsep, K. Timpmann and G. Trinkunas, *Dual fluorescence of single lh2 antenna nanorings*, *J. Lumin.* **108** (2004) 107–110. 39
- [39] S. Jang, E. Rivera and D. Montemayor, *Molecular level design principle behind optimal sizes of photosynthetic lh2 complex: Taming disorder through cooperation of hydrogen bonding and quantum delocalization*, *J. Phys. Chem. Lett.* **6** (2015) 928–934. 39
- [40] M. T. Sajjad, A. Ruseckas and I. D. Samuel, *Enhancing exciton diffusion length provides new opportunities for organic photovoltaics*, *Matter* **3** (2020) 341–354. 39
- [41] Y. Firdaus, V. M. Le Corre, S. Karuthedath, W. Liu, A. Markina, W. Huang et al., *Long-range exciton diffusion in molecular non-fullerene acceptors*, *Nat. Commun.* **11** (Oct, 2020) 5220. 39
- [42] S. J. Jang, *Robust and fragile quantum effects in the transfer kinetics of delocalized excitons between b850 units of LH2 complexes*, *J. Phys. Chem. Lett.* **9** (2018) 6576–6583. 39
- [43] J. Strümpfer, M. Şener and K. Schulten, *How quantum coherence assists photosynthetic light-harvesting*, *J. Phys. Chem. Lett.* **3** (2012) 536–542, [<https://doi.org/10.1021/jz201459c>]. 40

- [44] S. Baghbanzadeh and I. Kassal, *Geometry, supertransfer, and optimality in the light harvesting of purple bacteria*, *J. Phys. Chem. Lett.* **7** (2016) 3804–3811, [<https://doi.org/10.1021/acs.jpclett.6b01779>]. 40
- [45] S. Baghbanzadeh and I. Kassal, *Distinguishing the roles of energy funnelling and delocalization in photosynthetic light harvesting*, *Phys. Chem. Chem. Phys.* **18** (2016) 7459–7467. 40
- [46] W. Strek, *Cooperative energy transfer*, *Phys. Lett. A* **62** (1977) 315–316. 40
- [47] G. D. Scholes, *Designing light-harvesting antenna systems based on superradiant molecular aggregates*, *Chem. Phys.* **275** (2002) 373–386. 40